POLITECNICO
MILANO 1863

SCUOLA DI INGEGNERIA INDUSTRIALE
E DELL'INFORMAZIONE

Preliminary analysis of an autorotational Airborne Wind Energy system

Tesi di Laurea Magistrale in
Aeronautical Engineering - Ingegneria Aeronautica

Author: **Luca Cominoli**

Student ID: 952906
Advisor: Prof. Alessandro Croce
Co-advisor: Dott. Filippo Trevisi
Academic Year: 2021-2022

Gutta cavat lapidem non vi,
sed saepe cadendo.

Lucrezio

Abstract

Autorotation has been a well-known principle for a century, when, at the beginning of the twentieth century, Juan de la Cierva began studying it for the construction of the first rotary-wing aircraft: the gyroplane. Autorotation is a phenomenon whereby a rotor, hit by a relative wind, is able to generate lift and torque applied to the shaft. This phenomenon is widely used in the aeronautical field: it is the basis of the gyroplane and it is also exploited by helicopters, in case of engine failure, to slow down the descent. These are not the only applications, in fact, starting from 1980, it was taken up by Roberts [1] who proposed its use for the production of electricity by exploiting the winds at high altitudes. This thesis is based on the Roberts' idea and is part of the Airborne Wind Energy (AWE) world, which includes all the technologies for the production of electricity. Despite the advantages of autorotational AWE, there are no data in literature regarding rotor powers, weights and dimensions that characterize this system. In this context, this thesis is intended with the aim of reducing this lack of data in the literature and providing greater interest in such technology. In particular, the aim is to identify the weight and size of the rotor required to produce three different electrical power: 5, 30 and 100 kW. These values represent the typical powers of the most popular AWE systems (*Kitemill* of 5.5 and 100 kW [2, 3], *Skypull* of 25 kW [4] and *SkySails* of 200 kW [5]). They are also chosen to explore the parameters required to obtain powers on a scale of two orders of magnitude. For this purpose, at first, the model of autorotation, developed by Rimkus and Das [6], is described; then the structural model is developed. This model is very simple and was created specifically for the study of a system with two counter-rotating rotors connected by a beam which in turn is constrained to the ground. This simple model is used to perform a parametric analysis with approximately 200 000 different designs. Finally, the data produced by this analysis are used to obtain general indications about the effects of the design variables on the power and on the wind speed required for steady state operation. This indications are then used to extract a design for each of the three power sizes which in turn are studied in greater detail in order to introduce further improvements.

Keywords: airborne wind energy; AWE; autorotation; autogyro; wind energy; high altitude winds.

Abstract in lingua italiana

L'autorotazione è un principio ben noto da ormai un secolo, quando, a inizio Novecento, Juan de la Cierva iniziò a studiarlo per la realizzazione del primo velivolo ad ala rotante: l'autogiro. L'autorotazione è un fenomeno per cui, un rotore, investito da un vento relativo, è in grado di genereare portanza e una coppia all'albero. Questo fenomeno, largamente utilizzato in campo aeronautico, è alla base dell'autogiro ed è anche sfruttato dagli elicotteri, in caso di avaria del motore, per rallentarne la discesa. Queste non sono le uniche applicazioni, infatti, a partire dal 1980, venne ripreso da Roberts [1] che ne propose l'utilizzo per la produzione di energia eolica. Questa tesi è basata sull'idea di Roberts e si colloca nel settore di Airborne Wind Energy (AWE) che comprende tutte quelle tecnologie che sfruttano i venti ad alta quota per la produzione di energia elettrica. Nonostante i vantaggi di un sistema AWE autorotazionale, questa tecnologia è stata poco studiata e, in letteratura, non sono presenti dati riguardanti potenze, pesi o dimensioni dei rotori tipici di tale sistema. In questo contesto, si colloca quindi questa tesi con l'obiettivo di ridurre la mancanza di informazioni e suscitare nuovo interesse per questa tecnologia. In particolare, l'obbiettivo consiste nel determinare il peso e la dimensione dei rotori di 3 diverse configurazioni da 5, 30 e 100 kW di potenza, valori tipici dei più diffusi sistemi AWE (Kitemill da 5.5 e 100 kW [2, 3], Skypull da 25 kW [4] e Skysails da 200 kW [5]). Oltre a ciò, queste tre configurazioni sono state scelte per esplorare i parametri richiesti per ottenere potenze su una scala di 2 ordini di grandezza. Si inizia, quindi, descrivendo il modello aerodinamico di autorotazione, introdotto da Rimkus e Das [6]. In seguito, il modello strutturale è sviluppato appositamente per un sistema con due rotori controrotanti, collegati da una trave, e vincolato a terra tramite un cavo. Questo semplice modello, è poi utilizzato per eseguire un'analisi parametrica che include circa 200 000 diversi design. Infine, i dati prodotti sono usati per ottenere indicazioni di massima, riguardo l'influenza dei parametri di progetto, su potenza e velocità del vento richiesta. Queste informazioni, sono poi utilizzate per estrarre un design per ciascuna delle tre taglie di potenza, ed in seguito, analizzate in dettaglio al fine di introdurre ulteriori miglioramenti.

Parole chiave: airborne wind energy; AWE; autorotazione; autogiro; energia eolica; venti di alta quota.

Contents

Introduction

Airborne Wind Energy (AWE) is a wind energy technology that is based on flying blades or wings attached to the ground by a tether [7]. This technology has been studied since the 19th century [8] with the aim of capturing the energy of the wind at high altitude, characterized by greater steadiness and greater power density, compared to that close to the ground. Although AWE is based on ideas born in two centuries of history, its foundation was only defined in 1980 thanks to Loyd's studies [9]. In fact, in these studies, he computed the maximum theoretical power that can be harvested with AWEs based on tethered wings [8]. In the early 2000s, this technology experienced strong growth with the birth of new companies in the AWE sector after the article published in 2009 by Archer and Caldeira as can be seen in Figure 1.

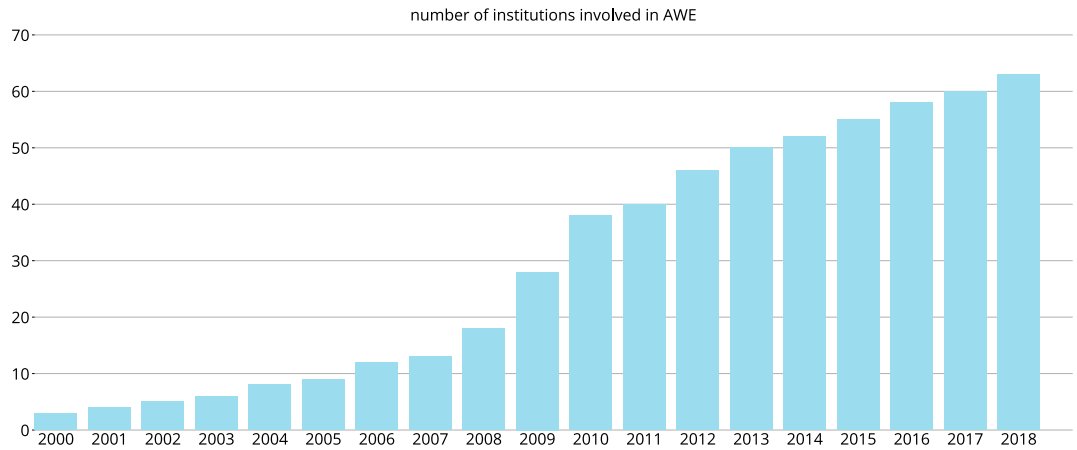

Figure 1: Number of AWE institutions in the early 2000s [10].

These two scientists, in fact, estimated the kinetic energy of the wind between 0.5 and 12 km of altitude and the results obtained increased the interest of researchers and companies for this technology. Subsequent studies tried to estimate the total power that can be extracted from the wind and, although the results were affected by great variability, the conclusion was the same: the entire world energy demand can be harvested only exploiting wind energy available in the atmosphere [8, 11].

It can be seen that in recent years, many companies and associations have taken an interest about Airborne Wind Energy (AWE) world. The interest has mainly focused on the crosswind method for wind energy harvesting and this phenomenon has led to the production of many bibliographic documents with different mathematical models and many results. It is important to notice that, the crosswind production isn't the only one applicable method, in fact, there are also other principles like autorotation. This last principle is less studied for energy harvesting and, for this reason, there are less bibliography that describes mathematical models and results. Therefore, there is little information to use when evaluating autorotational AWE performance. So, given the interest of companies in autorotation for energy production, this thesis is intended to provide a set of results that can compensate for the lack in literature about this technology. Furthermore, these results are used to provide guidelines for the preliminary sizing in terms of rotor radius and weight of AWE autorotation systems for different nominal power.

This thesis is divided into 5 chapters with the final conclusions. In the first chapter, the autorotation principle is introduced describing also its use in the AWE world. Subsequently, in chapter 2 the aerodynamic model, taken from [6, 12], is described while in chapter 3 the structural model for the verification of resistance and weight estimation is developed. These 2 models are then used to develop, in chapter 4, a low fidelity tool for a preliminary study of the autorotational AWE in order to produce the results shown in chapter 5. In this chapter, the developed tool is used to define 3 different designs capable of producing respectively 5, 30 and 100 kw of electrical power to understand how the size of the system changes for different nominal power. These 3 power values were chosen for two main reasons. These powers represent the typical values of AWE systems [2–5] with which a brief comparison will be made based on the few data available in the literature. Moreover, these power values cover approximately 2 orders of magnitude and are used to explore the effect of power on design variables. Finally, there are the conclusions in which the autorotational AWE system is compared with other AWE technologies also proposing improvements in the mathematical model and in this system to make it competitive.

1 | Introduction of autorotation in Airborne Wind Energy

It is well known that, the wind power density $P_d = \frac{1}{2}\rho V_w^3$ grows with the third power of the wind speed so that, a little increase in V_w, can generate an important increase in produced power. The disadvantage of the classical horizontal axis wind turbine is that, the rotor is mounted quite near the ground where is found the lowest wind speed in the atmosphere due to the presence of the boundary layer. In the atmospheric boundary layer, in fact, the wind speed grows with the distance from ground [13, 14] and, despite the decrease of the air density with height, the overall wind power density shows an increase [15]. Another problem of the wind energy is its intermittency. The wind speed, in fact, isn't constant over time so, as a consequence, it is not possible to control the power produced according to the demand with the drawback of having little power available during high demand periods. For what has just been said, starting from the 19th century, many scientists began to study methods to harvest high altitude wind energy [8] but, only in 1980 with Loyd [9], the foundations of this technology were established.

1.1. Airborne Wind Energy classification

Airborne wind energy is a technology created to produce wind energy trying to avoid the aforementioned problems that characterize classic wind turbines. This is achieved exploiting the greater power density and steadiness of high altitude winds as well as the possibility of controlling the operating altitude with the aim of maximizing the power produced. Over the years, different methods have been developed for the production of high altitude wind energy which can be classified according to three main characteristics:

1. electricity generation method;
2. flight operation;
3. the structure.

Figure 1.1 shows the classification with respect to the first two aspects with examples of companies that adopt each of the AWE strategies shown. The first classification concerns the method of producing electricity. The most widespread and studied solution is the one with a fixed generator [10] on the ground which is activated thanks to the tension of the tether connected to the kite. Other configurations use a ground station (connected to the kite with a cable) capable of moving and producing electricity through relative motion with respect to the ground. In the end, also the possibility of generating electrical power on the flying device is studied because, despite the grater weight of the AWE device, in this case it is possible to switch from generation to power mode. So it is possible to use electrical energy to control the flying device during the take off and landing.

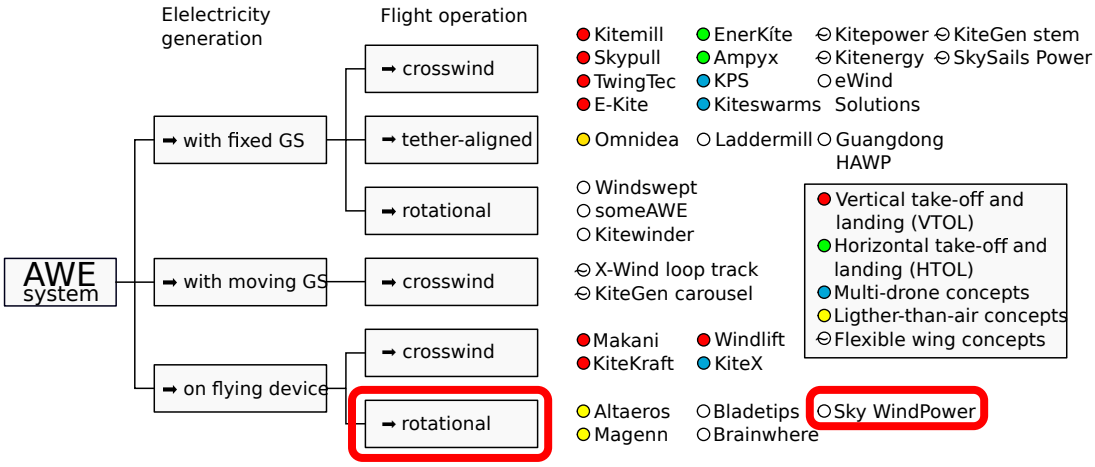

Figure 1.1: Airborne Wind Energy main classification [10].

The second classification of AWE systems is based on the flight operation mode where crosswind is the most widespread. In crosswind mode, the kite is controlled in such a way that it can move relative to the ground in order to increase the relative wind speed to the kite on which the aerodynamic loads depend. In this way, the kite is controlled to maximize the relative speed, hence the tether tension and consequently the electrical power produced. Than, tether-aligned flight operation include all the configuration that exploits aerodynamic loads without using crosswind and the **rotational flight operation** where, in addition to a traction force, a torque is also transmitted. This last classification also includes the flight operation that will constitute the technology studied in this thesis: the **autorotation**. In particular, the AWE system studied in this thesis is based on the rotational flight operation with electricity generation on the flying device; an example is the one made by *Sky WindPower* [16]. The last kind of classification is based on the structure, in fact, the flying device can have rigid or soft wings. In the first case the structure will be heavier but will have greater aerodynamic efficiency while, in the second

case, the structure will be lighter with lower aerodynamic efficiency. At the beginning of AWE technology, soft wings systems were the most popular for weight, cost and safety issues as, in the event of an impact, the damage would have been limited. On the other hand, even tough it is unclear which solution is the best, in the last period the trend is reversing with many companies moving towards the design of rigid wing systems [8].

In the end, based on these classifications, this thesis will focus on a flying generator system in rotational flight mode with rigid structure.

1.2. Principles of autorotation

The phenomenon of autorotation was discovered and studied for the first time in the early 1900s by Juan de la Cierva. In 1920, he managed to build the first model of a rotary wing aircraft with the rotor free to rotate with respect to the vertical axis. This discovery revolutionized the world of aeronautics by proposing a new lifting principle, different from that used in fixed-wing airplanes, and laid the foundations for the design of helicopters by anticipating their first successful flight by 15 years [17]. De la Cierva discovered the principle of autorotation after several accidents involving airplanes since their first invention in 1908 by the Wright brothers. De la Cierva's aim was, in fact, to create a safe and stable aircraft with also low stall speeds. About this ideas, de la Cierva wrote:

> "the wings of such an aircraft should be moving in a relation to the fuselage. The only mechanism able to satisfy this requirement is a circular motion [a rotor] and, moreover, in order to give adequate security to the aforementioned requirement it must be independent of the engine. It was thus necessary that these rotary wings were free-spinning and unpowered [18]."

With this purpose in mind, de la Cierva created this new type of aircraft with an unpowered rotor capable of producing lift when placed at positive angle of attack and equipped with a propeller to provide the necessary thrust.

In Figure 1.2 it is shown the comparison between the autogyro, also called gyroplane, and helicopter principles. In the autogyro, the rotor is unpowered and must be at positive angle of attack so that an upward flow passes through the rotor making it rotate with consequent production of lift. In addition to the rotor, an autogyro requires also a propeller that provide the required thrust to overcame the total drag. On the other hand, the helicopter rotor provides both the lift and the thrust but, given the torque applied to the rotor axis, it also requires a second small rotor to counteract that torque.

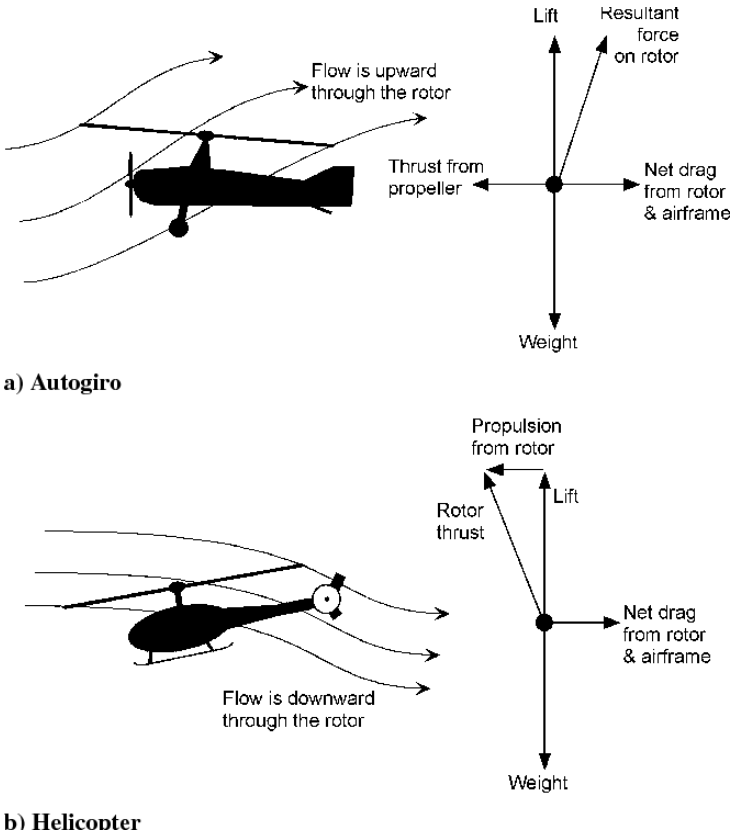

Figure 1.2: Forces acting on: a) autogyro and b) helicopter. Image taken from [17].

Now it is possible to understand the advantages of the autogyro against the helicopter. Autogyro is mechanically simpler than helicopter because it doesn't need engine gearbox and transmission toward the tail rotor resulting in weight savings, less maintenance and lower costs. Moreover, the gyroplane has characteristics that act as a bridge between airplane and helicopter given that operates like an airplane and it can't hover but it has a very low stall speed and it is capable of landing and taking off in small spaces. Last but not least, there is the safety aspect of gyroplane. It's normal operation condition, in fact, is autorotation so, in case of engine failure, it can land safely exploiting this principle. On the other hand, the normal operation condition of the helicopter is different and autorotation is used only in case of emergency to slow down the descent.

1.2.1. Physics of autorotation

Autorotation is a state of flight characterized by a self sustained rotation of the main rotor without the application of any resultant of shaft torque ($Q = 0$). In this condition the rotor is kept sustained by the air passing through the disc instead of the torque produced by the engine [17, 19]. In order to understand the principle of autorotation, it is useful

to understand how lift and drag vary as a function of the inflow angle ϕ_r of the blade through Figure 1.3 where:

$$\phi_r = \frac{\text{Upflow velocity}}{\text{In plane velocity}} = \arctan\left(\frac{|\mathrm{V}_c + v_i|}{\Omega r}\right) \tag{1.1}$$

while V_c is the climb velocity, v_i is the average induced velocity through the rotor, Ω is the rotor angular velocity and r is the radial position. In fact, the definition of autorotation requires that the total torque on the rotor shaft must be zero and this is obtained for a particular value of the inflow angle ϕ_r such that:

$$D - \phi_r L = 0 = C_D - \phi_r C_L \tag{1.2}$$

with D the airfoil drag and L its lift force.

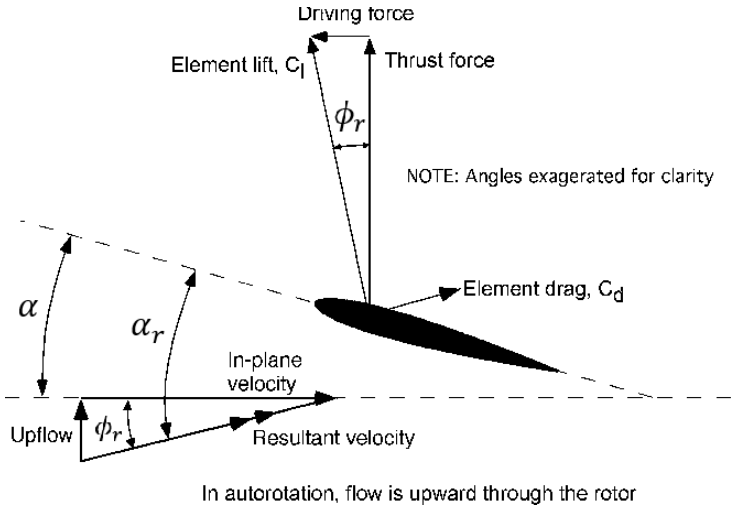

Figure 1.3: Relative flow to the blade element with also lift and drag direction as function of the inflow angle ϕ_r [17]

However the condition in Eq.(1.2) can be satisfied only for a certain section of the blade which will be called in autorotational equilibrium and which divides the blade in two regions: the inner one that absorbs energy from wind and the external one, closer to the tip, which consumes power. In the **inner region**, the lower value of *in plane velocity* produces a greater value of ϕ_r (see Figure 1.3) and consequently a greater angle of attack $\alpha_r = \alpha + \phi_r$ where α is the pitch angle of the blade section. So, in this region, the resulting angle of attack produces a forward inclination of lift. In turn, it produces a driving force greater than the airfoil drag component in the horizontal plane, resulting in overall positive torque. It is precisely this torque, that is generated as consequence of the

passage of the fluid, that keeps the rotor in rotation.

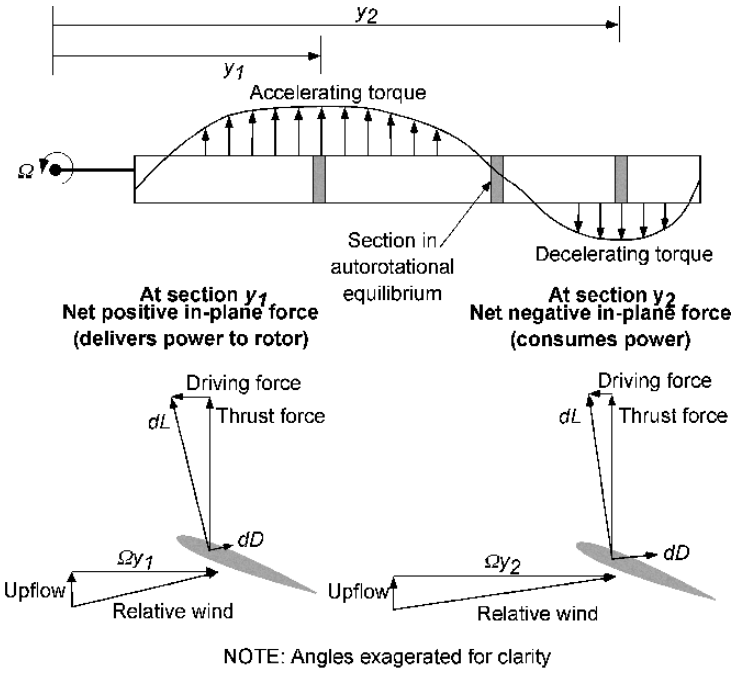

Figure 1.4: Forces acting on a blade in autorotation equilibrium for which the net torque on the rotor shaft is zero [17]

On the other hand, the **external region** of the blade consumes energy because, the lower inflow angle ϕ_r produces lift with a small driving force (it is the in-plane component of lift) that isn't enough to overcome the airfoil drag. So, given that this part is dominated by drag, in this region, the energy produced in the inner part of the blade is consumed. This physical phenomenon is stable in fact, during autorotation, the rotor speed Ω adapts to have a balance on the shaft with the resultant of the torque equal to 0. In case of an increase of Ω, the inflow angle decreases causing the extension of the dissipative region and producing a slowing down of the angular velocity of the rotor. Conversely, a decrease of Ω will produce an increase in inflow angle resulting in an extension of the region that extracts power from the flow causing an increase of Ω. This characteristic of intrinsic stability of this phenomenon makes all aircraft that use it, such as gyroplanes, particularly safe and for this reason this principle has been widely studied to be applied also to helicopters in case of engine failure.

1.3. Autorotation in airborne wind energy

Following what has just been said, autorotation is a widely studied physical phenomenon with a long history: it allowed the construction of the first rotary wing aircraft and laid the foundations for the design of helicopters. Although gyroplanes are not as common today as helicopters, the underlying physical principle is still fundamental to the safety of an helicopter and is used in the event of an engine failure [20]. In addition to this, the principle of autorotation has returned of interest among the scientific community after Roberts's 1980 paper [1] in which he proposed to exploit it for the design of systems for the production of high-altitude wind energy.

After this preliminary study, the collaboration between Roberts and the *Sky WindPower* [16] company led, in 1986, to the realization and consequent test of the first AWE system prototype at the University of Sydney shown in Figure 1.5. After these tests, Roberts' studies continued allowing to refine the first prototype giving rise to a 4-rotor system designed to operate at an altitude of 4600 m [21] described also in other works ([22, 23]). Despite these advances in the field of autorotation for high-altitude power generation, both Sky WindPower and Roberts abandoned the project.

Figure 1.5: Test of the prototype created by the collaboration between *Sky WindPower* and Roberts. Photo taken in May 1986 [24].

It was only several years later that the principle of autorotation in the AWE world was re-evaluated thanks to the analysis of Mackertich and Das in their work published in 2016 [25]. In this study, the two scientists analyzed all existing AWE designs and noted that the research was limited to applications for relatively low altitudes ($<$1 km)[25, 26]. Although the studies showed that above 5 km of altitude very high power densities could be found which could have made this technology more competitive. With the aim of capturing

wind energy where high power densities are found, lighter than air, crosswind AWE, and tethered airfoil systems in general were considered arriving at the following conclusions. A tethered airfoil can be suitable and very efficient for low altitudes (<1 km) but, if you want to take advantage of the high power density of the wind at high altitudes, the best method is the use of autorotationl AWE systems. Autorotationl AWE, in fact, has several advantages over other AWE systems and classic wind turbines, such as:

1. Greater maneuverability;
2. High altitude energy production;
3. Ability to switch from generation to powered mode;
4. Greater altitude can be reached.

The greater maneuverability is a feature of all AWE with flying generator which also includes the autorotational AWE. This is due to the fact that the flying generator can be controlled in order to stabilize the aircraft but also it allows to mitigate the effect of wind variability. Unlike the classic fixed-altitude wind turbines, this system can move in a certain range of altitudes, allowing you to extend the working region and find the altitude that maximizes the electrical power produced. This is a great advantage because, although wind speed generally increases with altitude, depending on climatic conditions, the altitude at which maximum power density occurs can vary [13]. The second advantage of this technology is linked to the generation of electricity at high altitude. This allows to solve one of the typical problems related to the classic wind turbines: noise. In this case, in fact, the blades and the generator are at high altitude and this allows to considerably reduce the perceived noise and therefore reduce the acoustic impact. Also the noise produced by the tether is reduced compared to crosswind AWE given that, in autorotational AWE, the tether speed is lower. Another feature linked to the presence of the generator at high altitude rather than on the ground, is linked to the possibility of switching from production mode to powered mode, allowing both take-off and landing in the event of an emergency or too strong winds. Last but not least, there is the possibility of reaching very high altitudes, which require very long cables, since not working with crosswind, the tether contribution to drag force is much lower than in the crosswind case.

This study of the various AWE technologies has shown the strengths of autorotational AWE systems, allowing them to be re-evaluated to take advantage of the winds at even higher altitudes. From these studies, it can be deduced that it is worth continuing the research in this field and this thesis is intended to be a contribution towards this technology.

2 | Aerodynamic model for autorotational AWEs

In chapter 1, the world of AWE was presented paying particular attention to the principle of autorotation for the production of wind energy at high altitude. Although this technology has the advantages described in section 1.3, it has still been little studied and, in scientific articles, the principle has only been discussed as in [21] without a mathematical treatment. A mathematical model for autorotation has been developed for the first time in 1926 by Glauert in [12] but, only in 2013 a preliminary study to exploit this principle for wind power generation was conducted [6]. Then the mathematical model used in this thesis is described with all the simplifying hypotheses on which it is based. The model of the structure of the studied device will then follow, and finally, the validation of the developed Matlab script is performed with the use of data from [6].

2.1. Mathematical model of autorotation

The mathematical model used in this thesis is the one developed by Glauert in 1926 [12] for a single rotor of radius R, tilted backwards by an angle θ with respect to the horizontal. In this model, blades with constant chord c are considered and mounted to the hub with a small, positive and uniform pitch angle α. The model considers an air flow of speed V_w, parallel to the ground that hits the inclined rotor of angle θ, inducing a rotation speed Ω. This autorotational state produces aerodynamic loads which can be decomposed into the following components [12]:

- **T** is the thrust that is the upward force parallel to the rotor shaft,
- **H** is the longitudinal force which lies in the plane of the rotor and which is perpendicular to the thrust,
- **Y** is the lateral force, perpendicular to the other two forces and conventionally positive where the blades are advancing in the direction of motion.

Than, the lift (F_L) and drag (F_D) of an autogyro can be computed as follows, simply projecting the thrust and longitudinal force respectively on the perpendicular direction of the wind and along the wind direction. Than it is also possible to express these forces in therms of non-dimensional coefficients using $\pi \mathrm{R}^2$ and the wind speed V_w respectively as reference area and speed.

$$\begin{cases} F_L = \mathrm{T}\cos\theta - \mathrm{H}\sin\theta = k_L \pi \mathrm{R}^2 \rho \mathrm{V}_w^2 & \text{(2.1a)} \\ F_D = \mathrm{T}\sin\theta + \mathrm{H}\cos\theta = k_D \pi \mathrm{R}^2 \rho \mathrm{V}_w^2 & \text{(2.1b)} \end{cases}$$

Where k_L and k_D are the lift and drag coefficients of the rotor. All the aforementioned loads and geometric properties of the autogyro are shown in Figure 2.1.

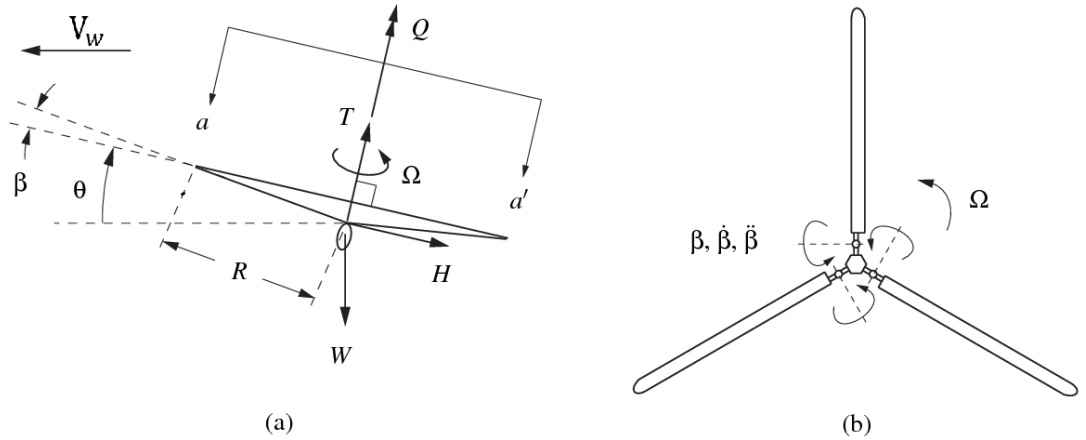

Figure 2.1: (a) Loads on the autogyro (weight W included) with geometric parameters. (b) View from the top of the rotor (aa′).

The position of each blade is defined using two different angles:

- β is the coning angle. It is the angle between the blade and the plane of the rotor;
- ψ is the blade's angular position (azimuth). It is equal to zero when the blade is aligned with the flow and is about to enter in the advancing region.

In this model developed by Glauert, the coning angle is assumed to be a periodic function of the blade's angular position ψ and can be expressed in the form of the Fourier series as:

$$\beta = \beta_0 - \beta_1 \cos(\psi - \psi_1) - \beta_2 \cos(\psi - \psi_2) - \dots \tag{2.2}$$

At this point, it is possible to introduce an assumption for which the flapping oscillation

of the blade can be well described retaining only the first harmonics such that:

$$\beta = \beta_0 - \beta_1 \cos(\psi - \psi_1) \tag{2.3}$$

Furthermore, Glauert [12] introduced another parameter to describe the blade geometry: the χ parameter. This parameter is introduced to take in account the fact that, in general, the blades are curved downwards so, each blade element at different radial position have different β angle. This angle is defined as:

$$\chi = \frac{\mathrm{d}d_b}{\mathrm{d}r} \tag{2.4}$$

where d_b is the distance of the blade element from the line that goes from the root to the blade tip (see Figure 2.2). This angle represents the slope of the tangent line to the blade in radial position r.

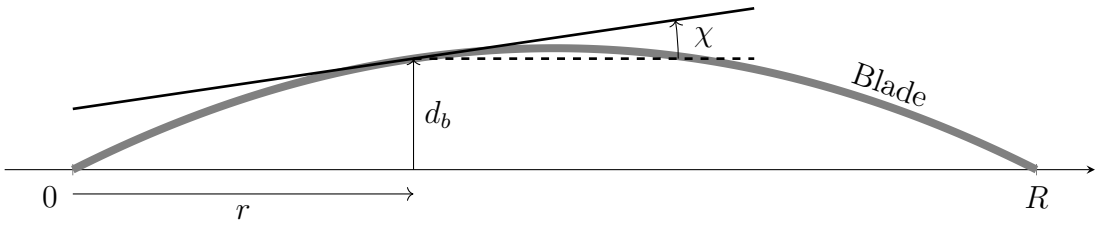

Figure 2.2: Angle χ: slope of the tangent to the blade at radial position r.

This model is based on the Blade Element Momentum theory for the calculation of thrust, torque and longitudinal force. So, a blade element in radial position r is considered and the aerodynamic forces applied to it are calculated and then integrated along the span of each blade.

2.1.1. Model hypothesis

In the next subsections, the procedure just described will be used to derive the formulas for thrust, longitudinal force and torque with the addition of the following assumptions:

1. The angles β and ϕ_r shown in Figure 2.3 are small;
2. The blades have an uniform chord c and constant pitch angle α;

3. The flapping motion is approximated retaining only the first harmonics (Eq.(2.3));

4. *Interference/Induced Flow*: near the rotor, the aerodynamic forces produce induced velocities that modify the airflow. This effect is modelled introducing an **induced axial velocity** ν. Than this induced axial velocity is assumed to be constant over the whole disc of the autogyro [12]. The induced axial velocity is computed starting from the thrust as follows:

$$\nu = \frac{\mathrm{T}}{(2\pi \mathrm{R}^2 \rho V')^2} \qquad \text{with} \tag{2.5a}$$

$$V' = \sqrt{(\mathrm{V}_w \sin\theta - \nu)^2 + \mathrm{V}_w^2 \cos^2\theta} \tag{2.5b}$$

   Than, this induced velocity, produced thanks to the third Newton's law, modify the **effective axial velocity** that enters in the rotor as follows:

$$u = \mathrm{V}_w \sin\theta - \nu \tag{2.6}$$

5. The blade radial velocity U_R (Figure 2.3) is ignored;

6. Given the small angles hypothesis, the lift coefficient of a blade element is assumed to be proportional to $\alpha_r = \alpha + \phi_r$ such that:

$$C_L = C_{L_{/\alpha}} \alpha_r \tag{2.7}$$

   where it is assumed $C_{L_{/\alpha}} = 3$. On the other hand, given the small angles hypothesis, the drag coefficient is assumed to be small with respect lift coefficient so, it can be replaced with a small and constant value, δ which represents an average drag coefficient of the airfoil [12, 27] as in Eq.(2.8).

$$C_D = \delta \tag{2.8}$$

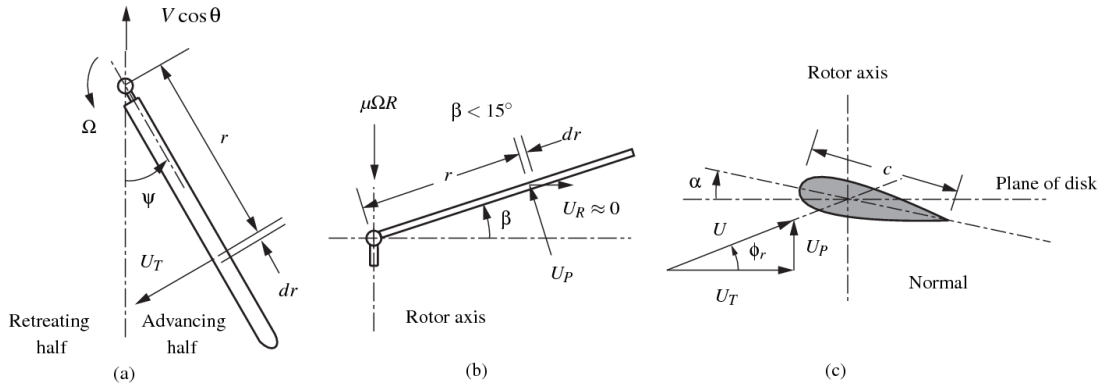

Figure 2.3: Airflow speed relative to a blade element. (a) view of the rotor plane, (b) view of flapping motion and (c) airflow speed from a cross-sectional view [6].

2.2. Aerodynamic loads

The aerodynamic loads applied to an autogyro can be expressed in therms of non-dimensional coefficients. In particular, using πR^2 and the tip speed ΩR as reference area and speed respectively, the following expression for the thrust T, longitudinal force H and torque Q can be obtained:

$$T = T_c \underbrace{\pi R^2}_{area} \rho \underbrace{\Omega^2 R^2}_{speed^2} = T_c \rho \pi \Omega^2 R^4 \tag{2.9}$$

$$H = H_c \rho \pi \Omega^2 R^4 \tag{2.10}$$

$$Q = Q_c \rho \pi \Omega^2 R^5 \tag{2.11}$$

Where T_c is the thrust coefficient, H_c is the longitudinal force coefficient and Q_c is the torque coefficient. Furthermore, also the blade element lift and drag can be expressed in therms of non-dimensional coefficients that are C_L and C_D as shown in the following:

$$D = \frac{1}{2} \rho U^2 \pi R^2 C_D \tag{2.12}$$

$$L = \frac{1}{2} \rho U^2 \pi R^2 C_L \tag{2.13}$$

Before moving on to the derivation of the formulas for T, Q and H, it is useful to determine the velocity of the flow incident to the blade, since, all the aerodynamic loads depend on this. To do this, Figure 2.3 is considered. Assuming that the radial velocity $U_R \approx 0$ and considering the usual approximation of small angles, the *relative velocity* U to a blade

element is:

$$U = \sqrt{U_P^2 + U_T^2} \tag{2.14}$$

where

$$\begin{cases} U_P = U \sin\phi_r = u - r\dot{\beta} - (\beta + \chi) V \cos\theta \cos\psi & \text{(2.15a)} \\ U_T = U \cos\phi_r = \Omega r + V \cos\theta \sin\psi & \text{(2.15b)} \end{cases}$$

Using the relative velocity U and the area of an element ($c\,\mathrm{d}r$), the drag and lift forces acting on a blade element can be written as:

$$\mathrm{d}D = \frac{1}{2} C_D \rho U^2 c\,\mathrm{d}r \qquad \text{Drag} \tag{2.16}$$

$$\mathrm{d}L = \frac{1}{2} C_L \rho U^2 c\,\mathrm{d}r \qquad \text{Lift} \tag{2.17}$$

Furthermore, for the autogyro, two useful different speed ratios can be defined:

$$\lambda = \frac{V}{\Omega \mathrm{R}} \tag{2.18a}$$

$$\mu = \frac{u}{\Omega \mathrm{R}} \tag{2.18b}$$

where the *tip speed ratio* in Eq.(2.18a) represents the ratio between the wind velocity and the speed of the blade tip while, the *axial flow ratio* in Eq.(2.18b) represents the ratio between the inflow velocity and the tip speed. Now it is also possible to find a relation between the thrust and longitudinal force coefficients (T_c and H_c) with the lift and drag coefficients of the autogyro that are k_L and k_D as follows:

$$\begin{cases} k_L = \dfrac{\mathrm{T}_c \cos\theta - \mathrm{H}_c \sin\theta}{\lambda^2} & \text{(2.19a)} \\ k_D = \dfrac{\mathrm{T}_c \sin\theta + \mathrm{H}_c \cos\theta}{\lambda^2} & \text{(2.19b)} \end{cases}$$

2.2.1. Thrust force

Using the principle of the *Blade Element Momentum* theory, the steady state thrust force can be computed starting from C_L and C_D coefficients of each blade element as follows:

$$\mathrm{dT} = \mathrm{d}L \cos\phi_r + \mathrm{d}D \sin\phi_r \tag{2.20}$$

Following the hypothesis of small angles, $C_D \ll C_L$ and $\cos\phi_r \approx 1$, $\sin\phi_r \approx \phi_r$; the Eq.(2.20) becames $\mathrm{dT} = \mathrm{dL}$. So, using Eq.(2.7) with $C_{L_{/\alpha}} = 3$, Eq.(2.17) and $\mathrm{dT} = \mathrm{dL}$,

the thrust force over a single blade can be computed as:

$$\begin{aligned} dT_1 = \frac{1}{2}\rho U^2 C_L c\,\mathrm{d}r = \frac{1}{2}\rho U^2 3(\alpha+\phi)c\,\mathrm{d}r \\ = \frac{3}{2}\rho U^2(\alpha+\phi_r)c\,\mathrm{d}r \end{aligned} \tag{2.21}$$

This is the thrust produced by an element of a single blade. So, in order to compute the total thrust T, an integration along the blade span and for a complete rotation has to be performed.

$$\mathrm{T}_1 = \int_0^R \frac{3}{2}\rho U^2(\alpha+\phi_r)c\,\mathrm{d}r \tag{2.22}$$

Therefore, the total thrust for B blades with constant chord is computed as:

$$\mathrm{T} = \frac{\mathrm{B}}{2\pi}\int_0^{2\pi} d\psi \int_0^R \frac{3}{2}\rho c(\alpha+\phi_r)U^2\,dr \tag{2.23}$$

and, solving this integral, the total thrust T is obtained

$$\mathrm{T} = \mathrm{B}c\rho\Omega^2\mathrm{R}^3\left(\alpha+\frac{3}{2}\mu\right) \tag{2.24}$$

Furthermore, using Eq.(2.9), introducing the *rotor solidity* $\sigma = \frac{\mathrm{B}c}{\pi\mathrm{R}}$ and dividing Eq.(2.24) by $\rho\pi\Omega^2\mathrm{R}^4$, the thrust coefficient is obtained as:

$$\mathrm{T}_c = \sigma\left(\alpha+\frac{3}{2}\mu\right) \tag{2.25}$$

2.2.2. Aerodynamic torque

Here, the *Blade Element Momentum* theory is still used to compute the aerodynamic torque. In accordance with this theory, the torque produced by a blade element can be expressed as ([27]):

$$\mathrm{d}Q = (dL\sin\phi_r - dD\cos\phi_r)\,r \tag{2.26}$$

Than, introducing Eq.(2.7) with $C_{L_{/\alpha}} = 3$, Eq.(2.8) and Eqs.(2.17,2.16) the torque for a single blade with the small angles assumption can be expressed as:

$$\mathrm{d}Q_1 = \frac{1}{2}(C_L\phi_r - C_D)r\rho U^2 c\,\mathrm{d}r = \frac{1}{2}\rho c(3\alpha\phi_r + \phi_r^2 - \delta)U^2\,\mathrm{d}r \tag{2.27}$$

than the total torque for B blades of constant chord is computed as:

$$\mathrm{Q} = \frac{\mathrm{B}}{2\pi}\int_0^{2\pi} d\psi \int_0^{\mathrm{R}} \frac{1}{2}\rho c(3\alpha\phi_r + 3\phi_r^2 - \delta)U^2\,\mathrm{d}r \tag{2.28}$$

In the end, the resolution of this integral leads to the total aerodynamic torque of the rotor that is ([12]):

$$\mathrm{Q} = \mathrm{B}c\rho\Omega^2\mathrm{R}^4\left(\alpha\mu + \frac{3}{2}\mu^2 - \frac{1}{4}\delta\right) \tag{2.29}$$

Following a similar procedure used in 2.2.1 for the thrust, also the torque coefficient Q_c can be computed starting from Eq.(2.11) obtaining the following expression:

$$\mathrm{Q}_c = \mu\sigma\left(\alpha + \frac{3}{2}\mu\right) - \frac{1}{4}\sigma\delta = \mu T_c - \frac{1}{4}\sigma\delta \tag{2.30}$$

2.2.3. Longitudinal force

The longitudinal force applied on the autogyro can be computed using the *Blade Element Momentum* theory starting from the force on a blade element:

$$\mathrm{dH}_1 = \frac{\mathrm{dQ}_1}{r}\sin\psi - \mathrm{dT}_1(\beta + \chi)\cos\psi \tag{2.31}$$

replacing dT_1 and dQ_1 with Eq.(2.20) and Eq.(2.27) respectively and integrating along the blade span, the longitudinal force for a single blade is computed as:

$$\mathrm{H}_1 = \int_0^{\mathrm{R}} \frac{1}{2}\rho c\left[\frac{1}{r}(-3\alpha\phi_r - 3\phi_r^2 + \delta)\sin(\psi) - 3(\alpha + \phi_r)(\beta + \chi)\cos\psi\right]U^2\,\mathrm{d}r \tag{2.32}$$

while the longitudinal force produced by B blades with constant chord along the span is expressed by:

$$\mathrm{H} = \frac{\mathrm{B}}{2\pi}\int_0^{2\pi} d\psi \int_0^{\mathrm{R}} \frac{1}{2}\rho c\left[\frac{1}{r}(-3\alpha\phi_r - 3\phi_r^2 + \delta)\sin(\psi) - 3(\alpha + \phi_r)(\beta + \chi)\cos\psi\right]U^2\,\mathrm{d}r\,\mathrm{d}\psi \tag{2.33}$$

Solving this integral the longitudinal force is obtained:

$$\mathrm{H} = \mathrm{B}c\rho\Omega^2\mathrm{R}^3\left[\frac{1}{2}\delta + \frac{8}{3}\alpha^2 + \frac{13}{2}\alpha\mu + \frac{9}{2}\mu^2 + \frac{1}{12}\beta_0^2 + (8\eta_2 - 3\eta_1\beta_0) - 24\eta_2^2 + \frac{1}{2}\xi_1\right]\frac{\mathrm{V}_w\cos\theta}{\Omega\mathrm{R}} \tag{2.34}$$

where η_1, η_2 and ξ_1 are three parameters that completely represent the blade curvature (see [12]). So, given that the last terms in Eq.(2.34) depends on the blade weight and on the curvature, parameters known only after a detailed design, Glauert [12] proposed the following approximate formula for the longitudinal force coefficient H_c which depends on the average drag coefficient and pitch angle.

$$\mathrm{H}_c = \sigma\left(\frac{1}{2}\delta + \frac{8}{3}\alpha^2 + \frac{13}{2}\alpha\mu + \frac{9}{2}\mu^2\right)\frac{\mathrm{V}_w\cos\theta}{\Omega\mathrm{R}} = \sigma\left(\frac{8}{3}\alpha^2 + \frac{17}{2}\alpha\mu + \frac{15}{2}\mu^2\right)\frac{\mathrm{V}_w\cos\theta}{\Omega\mathrm{R}} \tag{2.35}$$

Using this approximate expression for H_c, the longitudinal force is computed as:

$$\mathrm{H} = \mathrm{H}_c\pi\rho\Omega^2\mathrm{R}^4 \tag{2.36}$$

2.2.4. Angular velocity and axial flow ratio

The discussion seen so far has allowed us to exploit blade element momentum theory to find expressions for T, H, Q but, in order to evaluate these loads, it is necessary to know μ and Ω. Now we will present the methods to calculate these two missing parameters and to be able to evaluate the aerodynamic loads on the rotor. To do this, the steady state condition is introduced for which, in this condition, the aerodynamic torque Q must be zero. So, using Eq.(2.29) and replacing $\mathrm{Q} = 0$ the following equation is obtained:

$$\begin{aligned} \mathrm{Q} = \mathrm{B}c\rho\Omega^2\mathrm{R}^4\left(\frac{1}{4}\delta - \alpha\mu - \frac{3}{2}\mu^2\right) = 0 \\ \implies \qquad \frac{1}{4}\delta - \alpha\mu - \frac{3}{2}\mu^2 = 0 \end{aligned} \tag{2.37}$$

Solving 2.37 and considering that only the positive value of μ has physical meaning, the axial flow ratio is computed as follows:

$$\mu = \frac{1}{3}\left[\sqrt{\alpha^2 + \frac{3}{2}\delta} - \alpha\right] \tag{2.38}$$

Than, in order to compute the angular rotor speed Ω, the thrust force expression is used in which $\mathrm{T} = \mathrm{T}_d$ where T_d is a design value for thrust.

$$T = \sigma(\alpha + \frac{3}{2}\mu)\pi R^4\rho\Omega^2 = \mathrm{T}_d \tag{2.39}$$

So, choosing a value for T_d the angular velocity of the rotor is :

$$\Omega = \sqrt{\frac{T_d}{\sigma(\alpha + \frac{3}{2}\mu)}\pi R^4 \rho} \tag{2.40}$$

2.2.5. Energy harvesting with autorotational AWE

For the energy harvesting, the steady state condition is considered with steady wind speed V_w parallel to the ground. Furthermore, to extract wind energy, an electrical generator is connected to the shaft and it produces an electric torque Q_e that decreases the steady state Ω (computed with $Q = 0$). For this reason, a different equation has to be set in order to compute the correct Ω during the energy production phase putting $Q = Q_e$ in Eq.(2.11) instead of $Q = 0$. Using also Eq.(2.30), this leads to the following equation:

$$\begin{aligned} Q &= \left[\mu\sigma\left(\alpha + \frac{3}{2}\mu\right) - \frac{1}{4}\sigma\delta\right]\pi R^5 \rho \Omega^2 \\ &= \left(\mu\sigma\alpha + \sigma\frac{3}{2}\mu^2 - \frac{1}{4}\sigma\delta\right)\pi R^5 \rho \Omega^2 \\ &= Q_e \end{aligned} \tag{2.41}$$

Than substituting the Eq.(2.40) for Ω:

$$\begin{aligned} &\left(\frac{3}{2}\sigma\mu^2 + \sigma\alpha\mu - \frac{1}{4}\sigma\delta\right)\pi R^5 \rho \frac{T_d}{Bc\rho R^3(\alpha + \frac{3}{2}\mu)} = Q_e \\ \implies \quad &\left(\frac{3}{2}\sigma\mu^2 + \sigma\alpha\mu - \frac{1}{4}\sigma\delta\right) = \frac{Q_e Bc\rho R^3(\alpha + \frac{3}{2}\mu)}{\pi R^5 \rho T_d} \end{aligned} \tag{2.42}$$

Finally, by collecting the terms in μ and μ^2 the following equation is obtained:

$$\frac{3}{2}RT_d\mu^2 + \left(\alpha RT_d - \frac{3}{2}Q_e\right)\mu - \left(\frac{1}{4}RT_d\delta + Q_e\alpha\right) = 0 \tag{2.43}$$

which is solved for μ instead of using Eq.(2.38).

2.3. Autogyro simulation

Once the mathematical model has been defined, in order to be able to study the performance of the autogyro, it is useful to define a procedure that, given the inputs, allows to calculate the applied loads and the electric power produced in a steady state. In this

thesis, the procedure developed in [6] is used and is shown below:

1. chose a target thrust force T_d and a given electrical torque Q_e;
2. chose a suitable range of values of $\tau = \lambda \cos\theta$. In particular, in this work, a range $\tau = [0; 0.8]$ is used to consider a range of theta between almost 5° to 90° of incidence;
3. solve for μ the Eq.(2.43) and compute Ω from Eq.(2.40);
4. compute T_c and H_c from Eq.(2.25) and Eq.(2.35) respectively;
5. it can be shown that :
$$\lambda \sin\theta = \mu + \frac{\frac{1}{2}T_c}{\sqrt{\mu^2 + \lambda^2 \cos^2\theta}} \tag{2.44}$$
so, solve for $\lambda \sin\theta$ for each value of $\tau = \lambda \cos\theta$.
6. now it is possible to solve for λ, θ, V obtaining a vector of λ value and a vector of V for each angle θ. This variable V is the required wind speed for steady state operation;
7. in the end k_L and k_D that are the lift and drag coefficients of the autogyro, can be computed using Eqs.(2.19). Now, from Eqs.(2.1), the lift and drag of the whole autogyro can be computed for each angle θ.

2.4. Autogyro model limitations

The model just described was built based on several simplifying assumptions as it is intended for use during the preliminary design. In this phase, in fact, it is required an algorithm that is capable of capturing the main physical phenomena and that is simple and fast in order to study many different configurations. Only in subsequent phases, in the detailed design, more complex and accurate models will be used for the analysis of secondary phenomena. As Glauert points out in [12], the assumptions underlying the model cease to be valid towards the part of the blade near the root and in a large area on the retreating blades. In fact, in these areas high ϕ_r angles are obtained, which makes the hypothesis of small angles fall away. Therefore, to avoid obtaining results with no physical meaning, the following **constraints** must be respected in every simulation ([6]):

1. U_T must be positive over the outer half of retreating blades implying that:
$$V_w \cos\theta < \frac{\Omega R}{2} \tag{2.45}$$

2. The outer half of the blade operates below the stall angle α_s such that it is required:

$$\alpha_r = \alpha + \phi_r < \alpha_s \qquad \text{for} \quad \frac{1}{2}\mathrm{R} \leq r \leq \mathrm{R} \quad \forall \psi \in [0, 2\pi] \tag{2.46}$$

3 | Structural model

In this thesis, as already said, an AWE system based on autorotation will be considered. In particular, instead of using just one rotor, two counter-rotating rotors connected by a beam will be used. This configuration is preferable because it allows to have a zero resulting torque which avoids twisting of the cable connected to the ground. After this, a simple structural model will be developed. It allows us to calculate the internal loads of the beam, which joins the two rotors, starting from the applied loads shown in Figure 3.1. In this figure the side view of the autorotational AWE is shown with $\mathrm{F_T}$, which is the total thrust force of two rotors, $\mathrm{F_H}$ which similarly represents the longitudinal force of two rotors and the total weight W_{tot} (structure, two motors and blades). Furthermore, the θ angle is the incidence of autogyro and ϵ is the inclination of the cable connected to the ground.

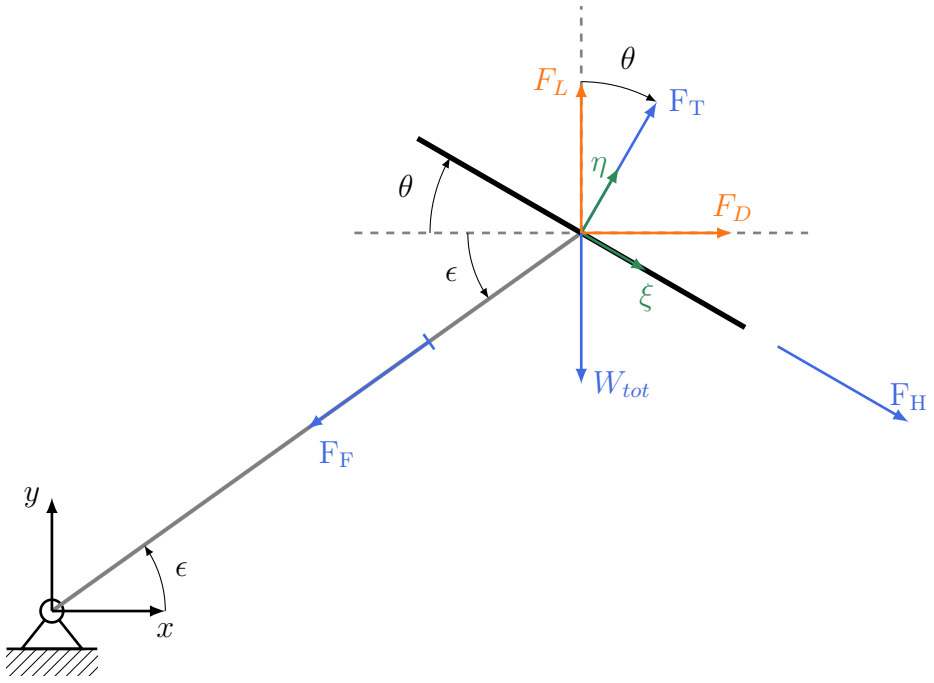

Figure 3.1: Side view (perpendicular to z axis) of the autorotational AWE system with the applied loads $\mathrm{F_T}$, $\mathrm{F_H}$ and W_{tot}

3.1. Tether force

In order to study the structure, which in this thesis is a simple beam, it is required to enforce the equilibrium and compute the tether tension, here called as $\mathrm{F_F}$.

$$\begin{cases} \overset{+}{\rightarrow} \sum F_x = \mathrm{F_T}\sin\theta + \mathrm{F_H}\cos\theta - \mathrm{F_F}\cos\beta = 0 \qquad \text{x-equilibrium} & (3.1a) \\ + \uparrow \sum F_y = \mathrm{F_T}\cos\theta - W_{tot} - \mathrm{F_H}\sin\theta - \mathrm{F_F}\sin\beta = 0 \qquad \text{y-equilibrium} & (3.1b) \\ + \circlearrowleft \sum M = 0 \qquad \text{rotational-equilibrium} & (3.1c) \end{cases}$$

By solving the system of equilibrium equations 3.1, it is possible to find the force in the rope $\mathrm{F_F}$ as in Eq.(3.2) and the angle ϵ in equilibrium conditions as shown in Eq.(3.3).

$$\mathrm{F_F} = \mathrm{F_T}\frac{\sin\theta}{\cos\beta} + \mathrm{F_H}\frac{\cos\theta}{\cos\beta} \tag{3.2}$$

$$\tan\epsilon = \frac{\mathrm{F_T}\cos\theta - W_{tot} - \mathrm{F_H}\sin\theta}{\mathrm{F_T}\sin\theta + \mathrm{F_H}\cos\theta} \tag{3.3}$$

Now the cable tension is known, so the positions of the cable attachments to the beam are defined. In particular, in the model it is assumed that the cable divides into 2 ropes at a distance d from the beam and connects in 2 points, at a distance a, from the ends of the beam itself as in Figure 3.2.

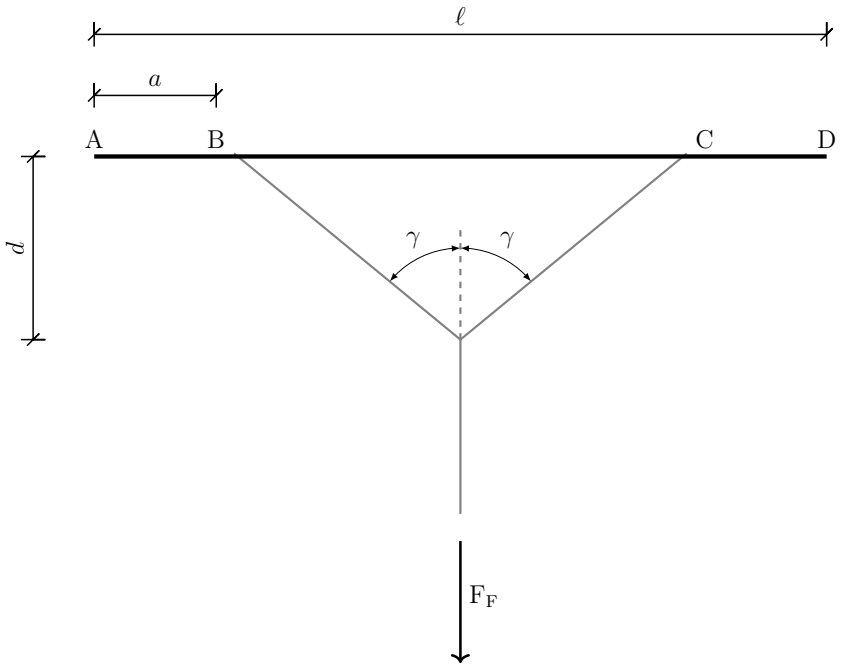

Figure 3.2: Parameters of cable attachments to the beam.

This configuration is preferred to the single attachment case, because it reduces the bending moment on the beam and consequently its weight. The last step to be done, before moving on to the calculation of the internal actions, is the calculation of the forces that the cable applies to the beam at the anchor points that are $\mathrm{F_{FB}}$ and $\mathrm{F_{FC}}$. To do this, Figure 3.3 will be taken as a reference where:

$$\gamma = \arctan\left(\frac{\frac{\ell}{2} - a}{d}\right) \tag{3.4}$$

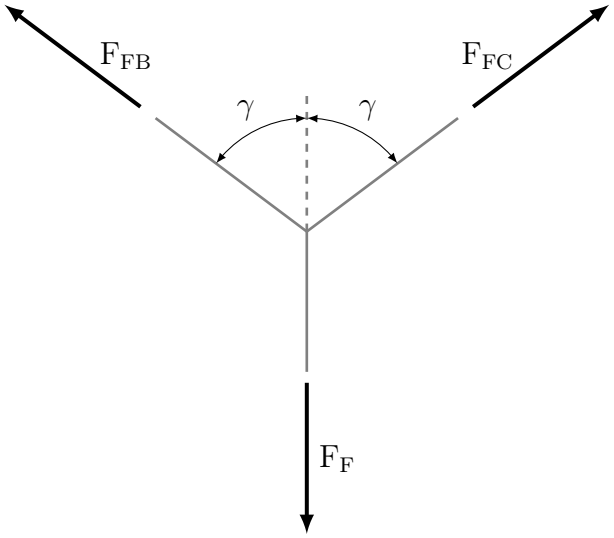

Figure 3.3: Forces acting on the bifurcation of the cable.

Once again the equilibrium equations are written to derive the forces exchanged with the structure as:

$$\begin{cases} \overset{+}{\rightarrow} \sum F_x = \mathrm{F_{FB}} \sin\gamma + \mathrm{F_{FC}} \sin\gamma = 0 & \text{x-equilibrium} \quad (3.5a) \\ + \uparrow \sum F_y = \mathrm{F_{FB}} \cos\gamma + \mathrm{F_{FC}} \cos\gamma - \mathrm{F_F} = 0 & \text{y-equilibrium} \quad (3.5b) \end{cases}$$

which once solved provides the expressions for the forces:

$$\mathrm{F_{FB}} = \mathrm{F_{FC}} \tag{3.6a}$$

$$\mathrm{F_{FB}} = \frac{\mathrm{F_F}}{2\cos\gamma} \tag{3.6b}$$

3.2. Model of the structure

The reference system of the beam, $(\xi - \eta - z)$, is defined with z directed from point A to D while, ξ and η axis are defined as in Figure 3.1. At this point it is possible to calculate the projection of the force in the two anchoring points to the beam with respect to the beam reference system. The forces in point B are the following:

$$\mathrm{F}_{\mathrm{B}z} = \mathrm{F}_{\mathrm{B}} \sin\gamma \tag{3.7a}$$

$$\mathrm{F}_{\mathrm{B}\xi} = -\mathrm{F}_{\mathrm{B}} \cos\left(\beta + \theta\right) \tag{3.7b}$$

$$\mathrm{F}_{\mathrm{B}\eta} = -\mathrm{F}_{\mathrm{B}} \cos\gamma \sin\left(\beta + \theta\right) \tag{3.7c}$$

while, for symmetry, in point C the forces are:

$$\mathrm{F}_{\mathrm{C}z} = -\mathrm{F}_{\mathrm{B}} \sin\gamma \tag{3.8a}$$

$$\mathrm{F}_{\mathrm{C}\xi} = -\mathrm{F}_{\mathrm{B}} \cos\left(\beta + \theta\right) \tag{3.8b}$$

$$\mathrm{F}_{\mathrm{C}\eta} = -\mathrm{F}_{\mathrm{B}} \cos\gamma \sin\left(\beta + \theta\right) \tag{3.8c}$$

As already mentioned, the structure consists of a simple beam which connects the two rotors allowing the loads, produced by them, to be transferred to the ground via the cable. Figure 3.4 shows the diagram of the structure considered with the applied loads. In this figure, W_η represents the distributed weight of the beam while W_s the total beam weight. F_η, in plane $\eta - z$, represents the vertical force in A and D given by the rotor thrust reduced by the component of rotor weight $W_R = W_m + \mathrm{B}W_B$ in that plane that is $(W_m + \mathrm{B}W_B)\cos\theta$ (W_m is the motor/generator weight, B the number of rotor blades and W_B the weight of a blade). Similarly for the plane $\xi - z$, F_ξ represents the longitudinal force corrected by the motor weight component in this plane.

$$W_\eta = \frac{W_s}{\ell} \cos\theta \tag{3.9a}$$

$$\mathrm{F}_\eta = T - W_R \cos\theta \tag{3.9b}$$

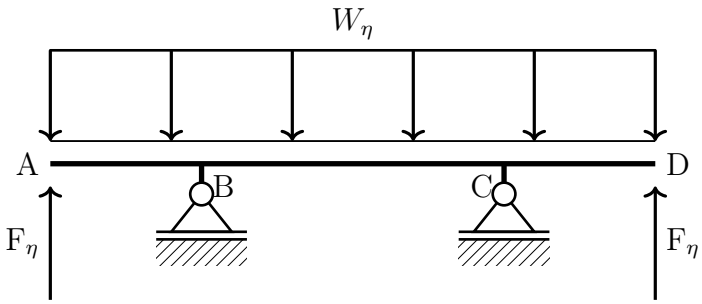

Figure 3.4: Model of the structure considered in this analysis. In particular, it is the taken from plane $\eta - z$.

3.2.1. Plane $\eta - z$

By removing the two constraints and replacing the constraint reactions, represented by the forces produced by the cable, it is possible to study the structure in plane $\eta - z$. The diagram in the Figure 3.5 is then obtained. Now, by imposing the equilibrium in each of the three beam sections ($\overline{AB}$, $\overline{BC}$, $\overline{CD}$), it is possible to find the diagrams of the internal actions using the convention shown in Figure 3.6.

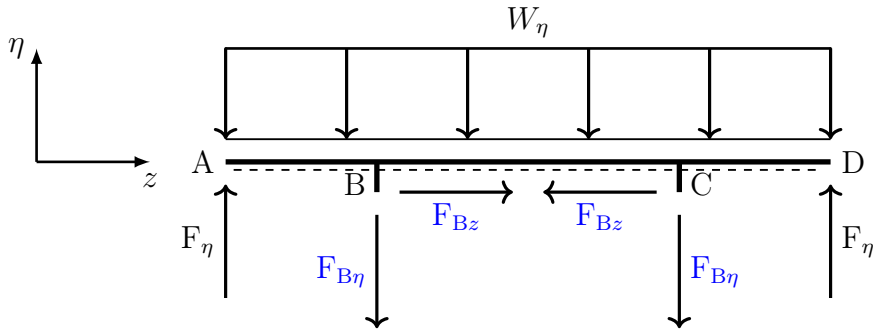

Figure 3.5: Loads and constraint reaction applied on the beam seen in plane $\eta - z$.

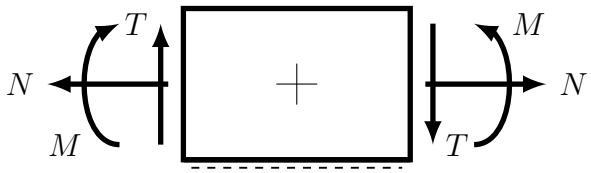

Figure 3.6: Internal action convention used to compute N, T and M.

Axial force

$$N(z) = \begin{cases} 0 & \text{in} \quad \overline{AB} \\ -\mathrm{F}_{\mathrm{B}z} & \text{in} \quad \overline{BC} \\ 0 & \text{in} \quad \overline{CD} \end{cases} \tag{3.10}$$

Shear force

$$T_\eta(z) = \begin{cases} -\mathrm{F}_{\mathrm{T}} + W_\eta z & \text{in} \quad \overline{AB} \\ -\mathrm{F}_{\mathrm{T}} + \mathrm{F}_{\mathrm{B}\eta} + W_\eta(a+z) & \text{in} \quad \overline{BC} \\ -\mathrm{F}_{\mathrm{T}} + 2\mathrm{F}_{\mathrm{B}\eta} + W_\eta(\ell - a + z) & \text{in} \quad \overline{CD} \end{cases} \tag{3.11}$$

Where the sign has been changed for the different convention of Figure 3.6 and the positive direction of η axis.

Bending moment

$$M_\xi(z) = \begin{cases} -\mathrm{F}_{\mathrm{T}} z + \frac{1}{2} W_\eta z^2 & \text{in} \quad \overline{AB} \\ -\mathrm{F}_{\mathrm{T}}(a+z) + \mathrm{F}_{\mathrm{B}\eta} z + \frac{1}{2} W_\eta (a+z)^2 & \text{in} \quad \overline{BC} \\ +\mathrm{F}_{\mathrm{B}\eta} z + \mathrm{F}_{\mathrm{B}\eta}(\ell - 2a + z) - \mathrm{F}_{\mathrm{T}}(\ell - a + z) + \frac{1}{2}(\ell - a + z)^2 W_\eta & \text{in} \quad \overline{CD} \end{cases} \tag{3.12}$$

Where the sign has been changed for the different convention of Figure 3.6 and the positive rotation around ξ axis.

3.2.2. Plane $\xi - z$

The same procedure is now used to study the effects of the applied loads in the $\xi - z$ plane shown in Figure 3.7. In this case, we will have a different expression for the distributed load (W_ξ), due to the weight of the structure (W_s). Furthermore in this plane, instead of

having F_η, we will have F_ξ. These two loads are defined as follows:

$$W_\xi = \frac{W_s}{\ell}\sin\theta \tag{3.13a}$$

$$\mathrm{F}_\xi = H + W_R \sin\theta \tag{3.13b}$$

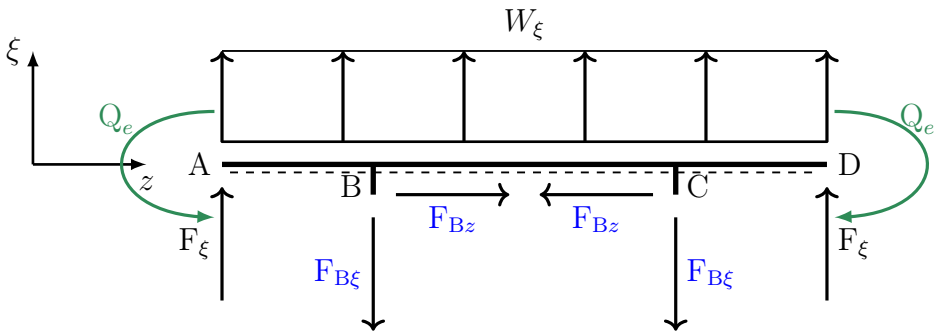

Figure 3.7: Loads and constraint reaction applied on the beam seen in plane $\xi - z$.

Axial force

$$N(z) = \begin{cases} 0 & \text{in} \quad \overline{AB} \\ -\mathrm{F}_{\mathrm{B}z} & \text{in} \quad \overline{BC} \\ 0 & \text{in} \quad \overline{CD} \end{cases} \tag{3.14}$$

Shear force

$$T_\xi(z) = \begin{cases} -\mathrm{F}_\xi - W_\xi z & \text{in} \quad \overline{AB} \\ -\mathrm{F}_\xi + \mathrm{F}_{B\xi} - W_\xi(a+z) & \text{in} \quad \overline{BC} \\ -\mathrm{F}_\xi + 2\mathrm{F}_{B\xi} - W_\xi(\ell - a + z) & \text{in} \quad \overline{CD} \end{cases} \tag{3.15}$$

Where the sign has been changed for the different convention of Figure 3.6 and the positive direction of ξ axis.

Bending moment

$$M_\eta(z) = \begin{cases} \mathrm{F}_\xi z + \frac{1}{2} W_\xi z^2 - \mathrm{Q}_e & \text{in } \overline{AB} \\ -\mathrm{F}_{B\xi} z + F_\xi (a+z) + \frac{1}{2} W_\xi (a+z)^2 - \mathrm{Q}_e & \text{in } \overline{BC} \\ -\mathrm{F}_{B\xi} (\ell - 2a + 2z) + F_\xi (\ell - a + z) + \frac{1}{2} (\ell - a + z)^2 W_\xi - \mathrm{Q}_e & \text{in } \overline{CD} \end{cases} \tag{3.16}$$

Here, the signs are unchanged because the convention in Figure 3.6 has a positive counterclockwise rotation as stated by η axis.

3.2.3. Axial stress in de Saint Venant's beam

In this thesis the beam model used is developed by de Saint Venant. In this model it is quite simple to compute the axial stress in the beam given the just computed internal actions diagrams. Using the Navier's formula, the axial stress σ_{zz} is obtained as:

$$\sigma_{zz} = \frac{N}{A} - \frac{M_\eta \xi}{I_{\eta\eta}} + \frac{M_\xi \eta}{I_{\xi\xi}} \tag{3.17}$$

Where $I_{\eta\eta}$ and $I_{\xi\xi}$ are respectively the beam section moment of inertia with respect η and ξ axis. This equation is used in order to verify the resistance condition of the beam: it must be verified that the axial stress σ_{zz} is always less than the *yield stress* of the material σ_y. In this thesis, the aforementioned equation (Eq.(3.18)) is verified in the 4 vertices of the section (A, B, C, and D) shown in Figure 3.8. Only these 4 points are considered because, from the Eq.(3.17), it can be noted that σ_{zz} increases with the distance from the *geometric center* and these 4 points are the most distant where the maximum value of the stress modulus is expected.

$$\sigma_{zz} < \sigma_y \tag{3.18}$$

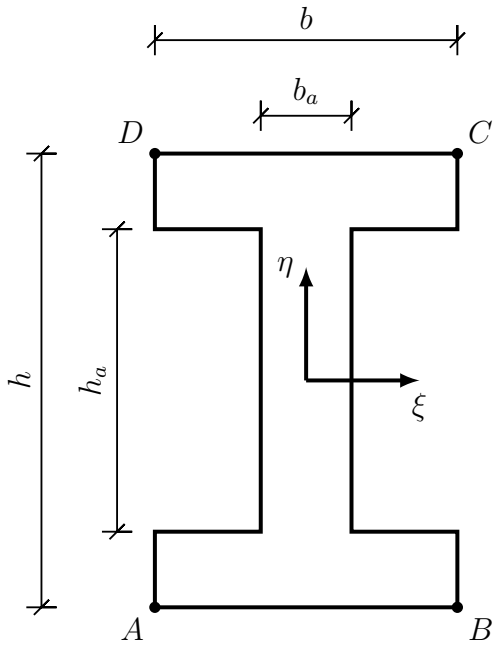

Figure 3.8: Beam section with input parameter in the structural script.

3.2.4. Euler's critical stress

The instability of the compression beam was also considered in the structural model. In fact, the beam will be very long since rotors with blades up to 5 m will be considered and which requires a beam longer than 10 m. In addition to this, it was also introduced to penalize designs where the distance a was very small (distance between the anchoring of the cables and the ends of the beam). These designs, in fact, are characterized by low bending moment but high compression force considering the same distance d.

The parameters that influence the Euler's instability, in addition to the type of material, are related to the geometry of the beam and are the *effective length* ℓ_E and the *slenderness* λ_E defined as follows:

$$\ell_E = \mu_c \ell \tag{3.19}$$

$$\lambda_E = \frac{\ell_E}{\rho_I} \tag{3.20}$$

where μ_c is a parameter that takes in account the kind of beam constraint, $\rho_I = \sqrt{\frac{I}{A}}$ is the *radius of gyration*. I is the *second moment of area* while A is the *cross-sectional area* of the beam. In order to compute the critical stress, it is only required the maximum value of slenderness that is:

$$\lambda_{E,max} = \frac{\ell_E}{\rho_{I_{min}}} = \frac{\mu \ell}{\rho_{I_{min}}} \tag{3.21}$$

with

$$\rho_{I_{min}} = \sqrt{\frac{I_{min}}{A}} \tag{3.22}$$

so, the critical stress depends on the lowest moment of inertia between $I_{\eta\eta}$ and $I_{\xi\xi}$. Now, the expression for the *critical stress* σ_{cr} can be written as:

$$\sigma_{cr} = \frac{E\pi^2}{\lambda_{E,max}^2} = \frac{E\pi^2\rho_{I_{min}}^2}{\ell_E^2} = \frac{E\pi^2 I_{min}}{\ell_E^2 A} \tag{3.23}$$

where E is the *Young's modulus* of the material.

In the structural model introduced in this thesis, we have a supported beam of length $\ell - 2a$ and for this type of constraint, $\mu_c = 1$ therefore $\ell_E = 1 \cdot (\ell - 2a)$. So, for this specific case, the critical stress is:

$$\sigma_{cr} = \frac{E\pi^2 I_{min}}{(\ell - 2a)^2 A} \tag{3.24}$$

In order to avoid Euler's instability, it is required to check that the axial stress between the two supports σ_N is:

$$\sigma_N < \sigma_{cr} \tag{3.25}$$

3.2.5. Blade structural analysis

The blades are a fundamental element of the rotor so, in this thesis, a model was used to verify their resistence against aerodynamic loads and to compute their mass: a fundamental parameter for this AWE system. In particular, the model used was developed thanks to the collaboration of the department of aerospace sciences and technologies of Politecnico di Milano and the DTU university of Denmark.

The model just mentioned considers a blade with a section composed of the twelve elements shown in Figure 3.9, where, each of them can be made with a different material. Among the most interesting outputs for this thesis are the axial stresses in the various structural elements for all sections along the blade and the mass of the overall blade. Regarding the axial stresses, only those in the spar caps will be considered since, in the preliminary design, only the bending strength, which is determined mainly by these two structural elements, will be considered.

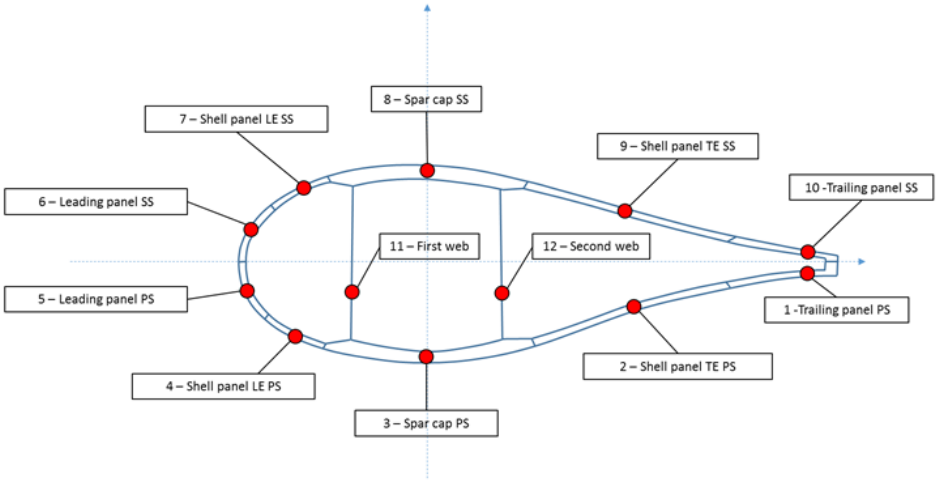

Figure 3.9: Blade section with 12 structural elements. The element 3 and 8 are the spar caps.

The blades considered in this thesis have a constant section therefore, for the purposes of the preliminary design, it is sufficient to use only 3 sections along the blade since the critical section will always be the one at the root. In this way the calculation time is reduced by eliminating the unnecessary sections for the hypothesis of constant section beam.

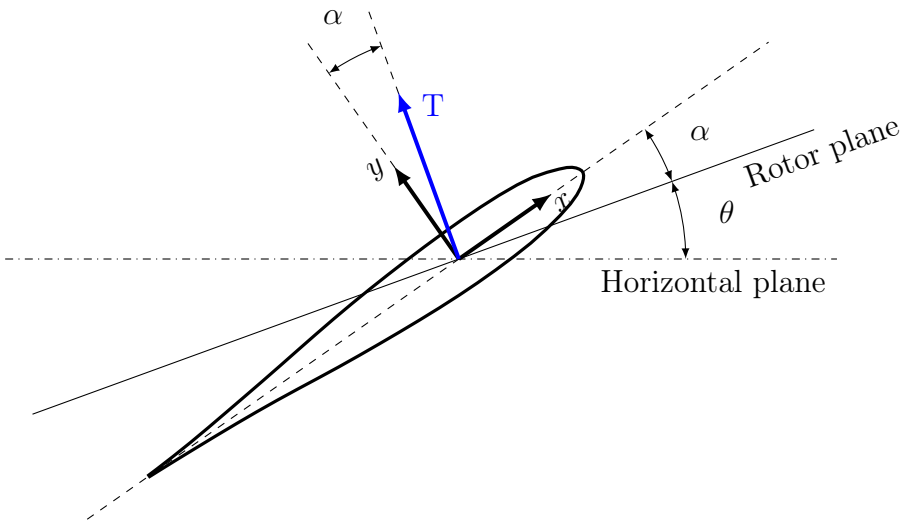

Figure 3.10: Side view of a blade element of GOE 429 airfoil with thrust force. The angles are not the real ones for graphic reasons.

Blade simulation

For the sizing of the blades, the vertical load that they must generate is considered since only a flapping sizing is performed. The total vertical load on each blade is calculated by dividing the thrust, that the rotor produces, by the number of its blades. Referring to Figure 3.10, it can be seen that the thrust component that generates flapping motion is $F_{y_{tot}} = \mathrm{T}\cos\alpha$ but, due to the hypothesis of small angles, it is reasonable to state that $F_{y_{tot}} \approx \mathrm{T}$ (in the following in fact $\alpha = 0.035$ rad). The force that produces the flap of each blade (F_y) is obtained by dividing $F_{y_{tot}}$ by the number of blades (B) as in Eq.(3.26).

$$F_y = \frac{\mathrm{T}}{\mathrm{B}} \tag{3.26}$$

Subsequently, a triangular distributed load along the blade is assumed in such a way that it has a resultant equal to the force F_y. Following this, the analysis of the internal actions of the blade, modeled as a cantilever beam, is performed. Considering also the coning angle of the blades, we note that only the component $\frac{\mathrm{T}}{\mathrm{B}}\cos\beta$ produces the bending but, for the hypothesis of small angles, it is assumed that:

$$F_y = \frac{\mathrm{T}}{\mathrm{B}}\cos\beta \approx \frac{\mathrm{T}}{\mathrm{B}} \tag{3.27}$$

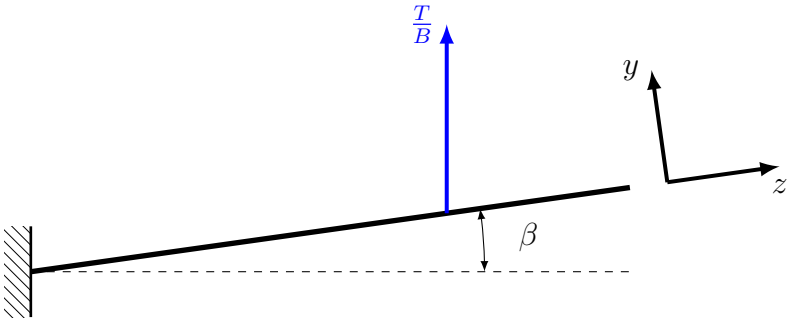

Figure 3.11: Side view of the blade.

At this point it is possible to carry out the calculation of the internal actions considering a triangular distributed load as in Eq.(3.28) such that its resultant is equal to F_y (see Figure 3.12).

$$q(z) = \frac{2F_y}{\mathrm{R}^2}z \tag{3.28}$$

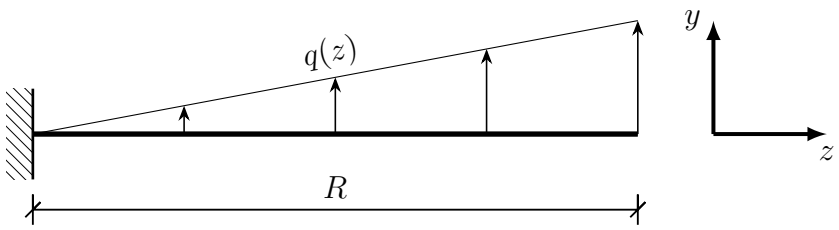

Figure 3.12: Load applied to the blade.

By imposing the equilibrium of the structure it is possible to obtain the graphs of the internal actions described by the following equations:

$$N(z) = 0 \tag{3.29a}$$

$$T(z) = \frac{F_y}{\mathrm{R}} z - F_y \tag{3.29b}$$

$$M(z) = \frac{1}{3}\frac{F_y}{\mathrm{R}} z^2 - F_y z + \frac{2}{3} F_y \tag{3.29c}$$

Among these equations, the 3.29c is the most important because it allows you to calculate the moments in the N_s sections into which the blade length is divided and use them as input for RotorCS. These moments, applied in the various sections, represent the bending load of the blade and are used to calculate the stresses in the spar caps and subsequently to compare them with the maximum allowable stresses of the material.

4 | Analysis of autorotational AWEs

In chapters 2 and 3 the mathematical model for the aerodynamics and for the structure have been described. The first model was taken from the work of Rimkus and Das [6], while, the second one was independently developed specifically for this thesis. In this chapter, these two mathematical models have been implemented using the Matlab software in order to produce data for a preliminary sizing of the AWE autorotational system. In fact, this Matlab script is used to produce data concerning about 200 000 configurations, from which, designs of 5, 30 and 100 kW are extracted and studied in further details.

In the following, the verification of the aerodynamic model is performed comparing the results, produced by the Matlab script, with those obtained by Rimkus and Das in [6]. Subsequently, the structure of the Matlab script will be described with all its features and then, the results produced will be shown.

4.1. Verification of the aerodynamic model

When writing code that implements a mathematical model, it is essential to verify that it executes the instructions correctly and that it produces the expected results based on the physics of the problem. So, for this reason, the developed script was used to solve the same problem as Rimkus and Das in order to be able to compare the results. The problem solved concerns the study of a rotor similar to that of the Pitcairn PCA-2; already studied by Wheatley [28] both from a numerical and an experimental point of view. The characteristics of the rotor, used in this comparison, are listed in Table 4.1.

After the first simulation, different plot are obtained. Then, the Matlab function, *grabit*, is used in order to extract some characteristic point from the plots in the article taken as a reference. Finally, the results shown in Figures 4.1, 4.2, 4.3 and 4.4 are obtained, where, the solid lines represent the results of the Matlab script while, circles, triangles and cross

symbols represent the data extracted from [6].

Parameter	Value	Value in SI	Description
ρ	0.0008 slugs/ft^3	0.4123 kg/m^3	Air density at 10 km of altitude
α	0.035 rad	0.035 rad	Blade pitch angle
δ	0.006	0.006	Mean airfoil drag coefficient
B	4	4	Number of blades
R	17.5 ft	5.33 m	Blade radius
Q_e	1000 lb·ft	1356 Nm	Electrical torque
T	2000 lbf	8896 N	Thrust
c	2.75 ft	0.838 m	Airfoil chord
Airfoil	-	-	GOE 429

Table 4.1: Parameter used in the simulation for the verification ([6]).

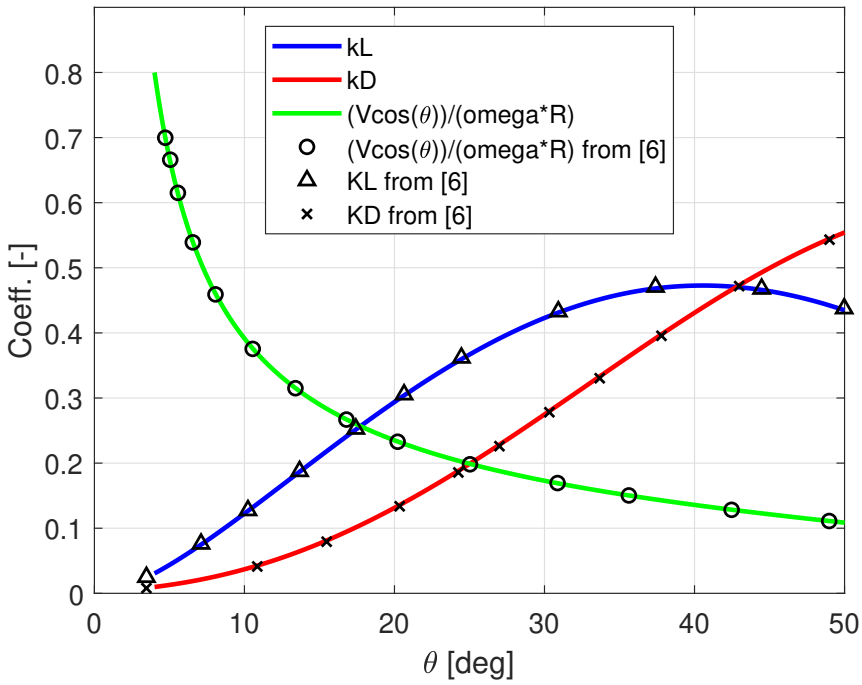

Figure 4.1: Aerodynamic coefficients of the autogyro with a model constraint (green line).

In Figure 4.1 the lift coefficient k_L, and drag coefficient k_D of the rotor are plotted for each value of the disc angle of attack θ. In the same figure, also one of the model constraint (see section 2.4) is plotted (green line) for which the validty of the results are limited for

all θ values at which the green line is below 0.5. From this figure it can be clearly seen that the results obtained are well in accordance with the reference data.

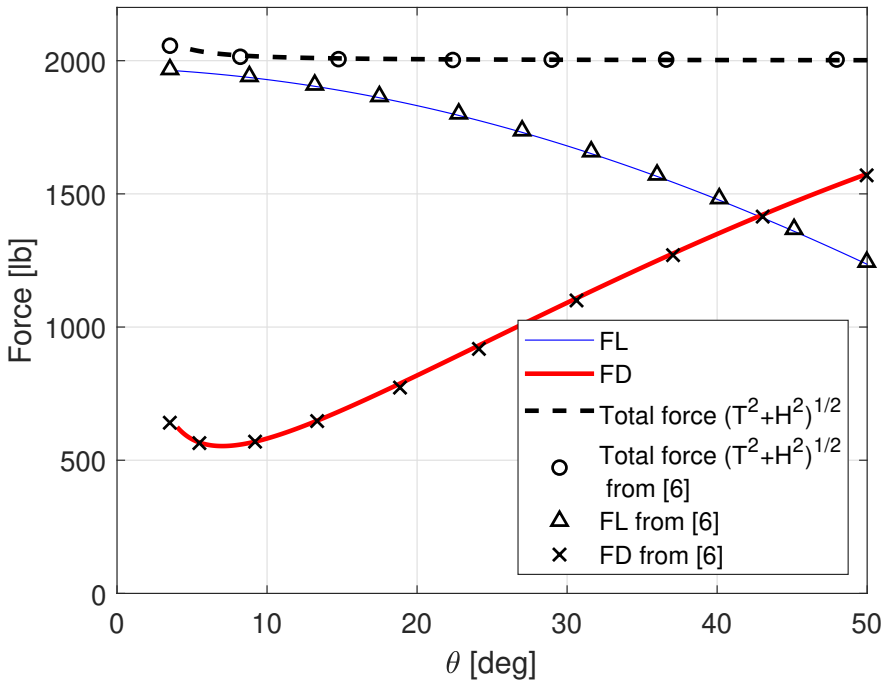

Figure 4.2: Aerodynamic loads of the autogyro.

In Figure 4.2 the aerodynamic load on the rotor are shown as a function of its angle of attack θ. The forces on the rotor are the thrust T and the longitudinal force H but, the lift F_L and the drag F_D can be obtained simply projecting T and H along the wind speed and in a perpendicular direction to it. Moreover the resultant force on the rotor is shown. Also in this case, a good correspondence is found between computed plot and reference data.

In order to operate in steady state conditions, autorotational AWE requires a certain wind speed that depends on θ. This requirement is shown in Figure 4.3 and, from the comparison with reference data, another successful outcome is obtained. Finally, also the electrical power and the angular velocity of the rotor are considered for the comparison. This result is shown in Figure 4.4 where good data overlap is found.

In the end, after all these successful comparison, it can be said that the **verification** has been passed and the script with the aerodynamic model can be used without introducing significant errors.

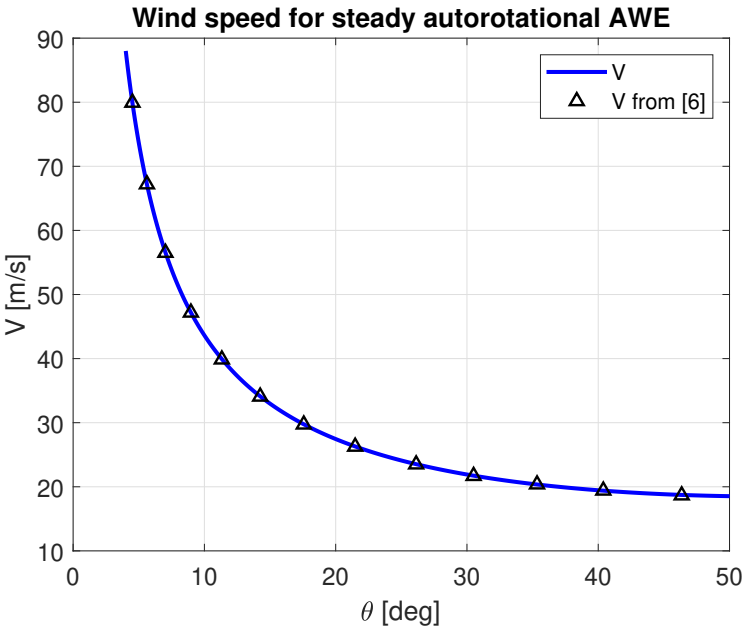

Figure 4.3: Wind speed required for steady state autorotational AWE.

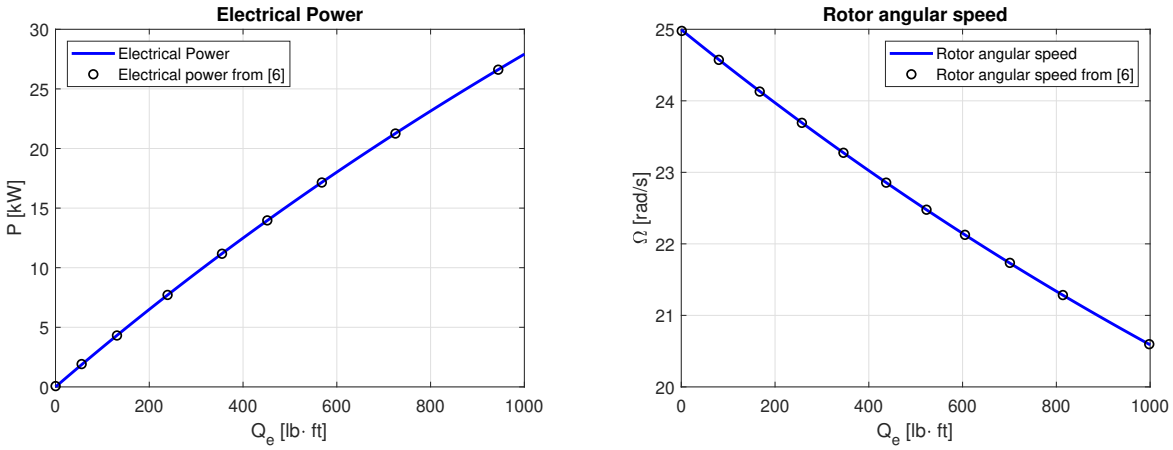

(a) Produced electrical power P.

(b) Angular speed of the rotor Ω.

Figure 4.4: Power (a) and angular speed (b) as function of electrical torque Q_e.

4.2. Matlab script structure and features

Before moving on to the results obtained, it is necessary to describe the organization of the developed script with its features. The developed script is mainly divided into two parts and it uses eight different function in order to check the 6 imposed constraints over several designs. The structure of the Matlab script is shown in Figure 4.5 and, in the following, both parts are briefly described.

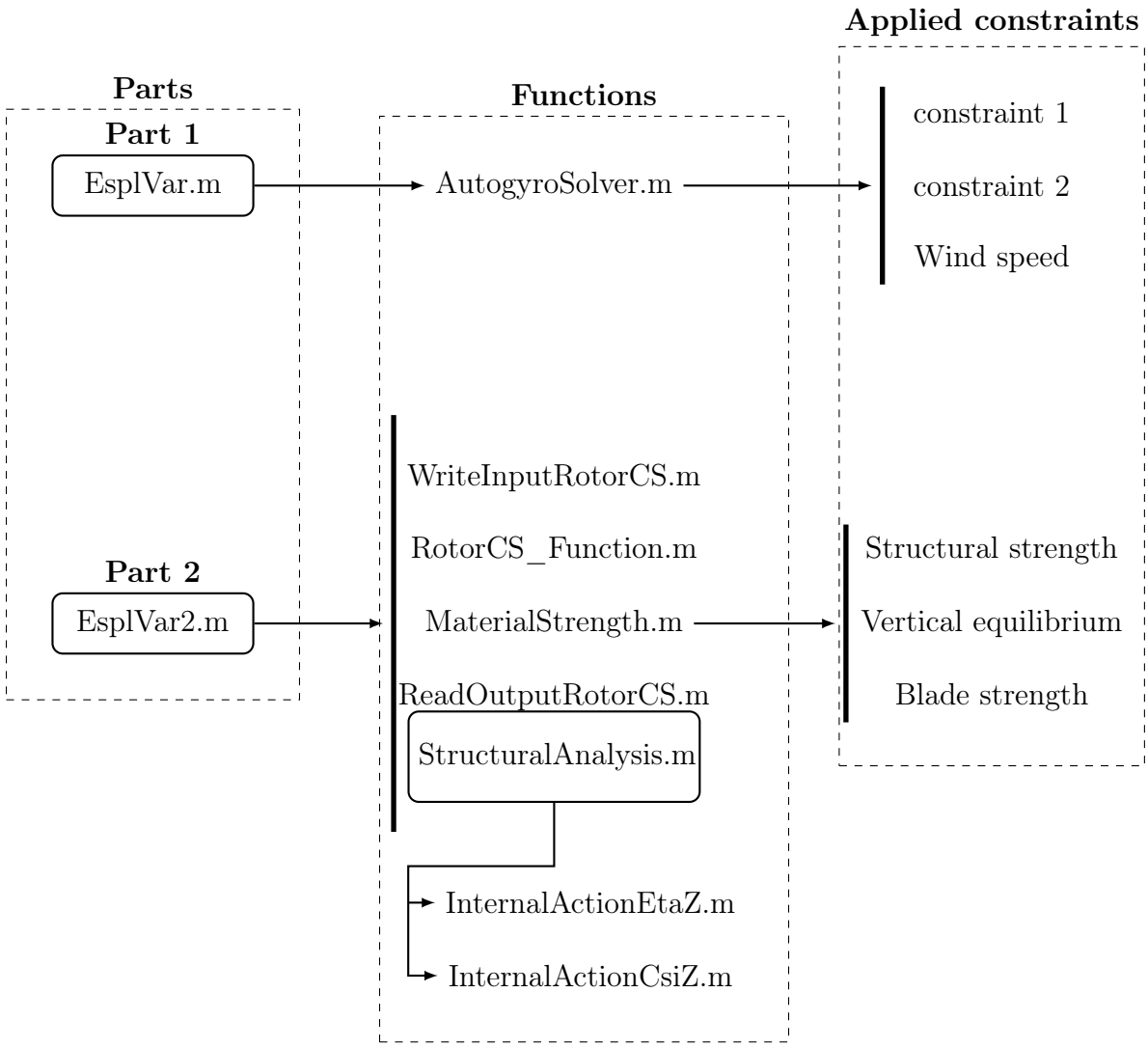

Figure 4.5: Structure of the script.

4.2.1. Part 1

The first part of the script, executed by the Matlab file `EsplVar.m`, can be defined as the "design generator". In this part, in fact, the inputs listed in Table 4.2 are set in order to create a large amount of hypothetical autorotational AWE designs to explore the space of parameters that defines this system. In addition to the parameters of the Table 4.2, the number of blades is also considered, but it is limited to design with 2, 3 and 4 blades.

Basically, this script performs a parametric analysis taking as input the vectors B, R, Q_e, T and c, then, for each combination, it calls the `AutogyroSolver.m` function. This function is the core of this script: it contains the aerodynamic model and is called several times in order to calculate the power produced by each design. In general, a large number

of designs, which depends on the size of the input vectors, can be obtained although not all of them have physical validity. It is important to remember that the aerodynamic model used is very simple and that it was obtained by applying several simplifying hypotheses.

Parameter	Description
δ	Mean airfoil drag coefficient
α	Blade pitch angle
ρ	Air density at 10 km of altitude
V_{max}	Maximum wind speed
α_s	Stall angle of the airfoil
R_{min}, R_{max}, $\Delta\mathrm{R}$	Used to define the blade radius vector $\mathrm{R}=[\mathrm{R}_{min} : \Delta\mathrm{R} : \mathrm{R}_{max}]$
Q_{min}, Q_{max}, $\Delta\mathrm{Q}_e$	Used to define the electrical torque vector $\mathrm{Q}_e=[\mathrm{Q}_{min} : \Delta\mathrm{Q} : \mathrm{Q}_{max}]$
T_{min}, T_{max}, $\Delta\mathrm{T}$	Used to define the thrust vector $\mathrm{T}=[\mathrm{T}_{min} : \Delta\mathrm{T} : \mathrm{T}_{max}]$
c_{min}, c_{max}, Δc	Used to define the chord length vector $c=[c_{min} : \Delta c : c_{max}]$

Table 4.2: Input parameters for EsplVar.m script.

As already discussed in section 2.4, in fact, to obtain physically valid results the following constraints must be satisfied:

Constraint C1: U_T must be positive over the outer half of retreating blades implying that:

$$\mathrm{V}_w \cos\theta < \frac{\Omega \mathrm{R}}{2} \tag{4.1}$$

Constraint C2: The outer half of the blade operates below the stall angle α_s such that it is required:

$$\alpha_r = \alpha + \phi_r < \alpha_s \qquad \text{for} \quad \frac{1}{2}\mathrm{R} \leq r \leq \mathrm{R} \quad \forall\psi \in [0, 2\pi] \tag{4.2}$$

In addition, **Constraint C3** is introduced to avoid inoperable configuration in practice: the maximum value of the minimum wind speed required for steady state operation, V_{max}. This was introduced because, in some cases, designs were generated with high power

production but which required minimum operating speeds that were too high (even 60 m/s). In order to better understand this constraint, it is useful to refer to the Figure 4.3 that represents the wind speed required for each θ angle for a fixed design. It can be noticed, that the required wind speed changes with θ, so, the minimum wind speed for each design is compared with V_{max}. If the minimum value of wind speed required for steady state is lower than a given V_{max}, the design can be considered, otherwise it is rejected because it works only for higher wind speed.

In the end, this first script creates many designs and can be said that it discards all those that cannot be used due to both model and atmospheric wind speed limitations. After this design selection, this script produces two important output that are:

1. `selected_design` variable that is a Nx6 matrix where N is the number of designs that have passed the three constraints. Each row of this matrix represents a design and contains, in order, the values of the following quantities: B, R, Q_e, T, c and the electrical power P produced.

2. `rejected_design` variable is a Mx9 matrix where M is the number of rejected designs. The first six parameters of each row are the same used in `selected_design` variable but, in this case, three more columns are added. Each column represents one of the three applied constraints and contains: 1 if a specific design has been rejected because it hasn't passed the constraint that corresponds to that specific column, while, 0 if the design has passed this constraint.

4.2.2. Part 2

We have just seen that the first part generates the designs and removes those that are not physically feasible: it is more general. The second part, on the other hand, considers the particular configuration of the autorotational AWE focusing on structural strength and vertical equilibrium.

This second part is carried out by the `EsplVar2.m` script which in turn calls several functions, described in the following, to analyze each design and apply the required constraints. This script starts by reading the `selected_design` variable, produced as output by the part just described, to apply also the other 3 required constraints. To do this, the `WriteInputRotorCS.m` function is called to modify the Excel file which constitutes the input for RotorCS. This is a script developed by DTU and Politecnico di Milano and used for the structural analysis of the blades. In particular, the aforementioned function changes the following parameter in the Excel file:

1. the flapping moments applied along the blade due to the aerodynamic loads;
2. the rotor and the hub radius;
3. the chord of the airfoil and scales the widths of the elements (seen from a direction perpendicular to the chord), which constitute the blade, to maintain similarity even with different chords;
4. it introduces a constant airfoil pitch along the blade.

After this, the `RotorCS_Function.m` can be run to solve the structural problem and compute the maximum stress in the blade and its mass. Thanks to the `MaterialStrenght.m` function, the spar caps material is found on the Excel input file with also its maximum admissible longitudinal, tensile and compressive, stress. Than, these values are compared with those obtained with `ReadOutputRotorCS.m` that are the maximum tensile and compressive stress in the spar caps of the blade. In the end, the `StructuralAnalysis.m` function is used in order to define the beam section (as in Figure 3.8), which connects two rotors, to compute its mass and, to assess if it satisfies the strength constraint.

At this point, for each design that has already passed the first three constraint, the mass of each blade and of the beam are computed. Than, the mass of the electrical motor is estimated knowing its power and using the conservative estimation of the power to weight ratio found in [29, 30] of 2.5 kW/kg. It is conservative because, higher values of this parameters can be found. Now, the last three constraint can be applied to each of the N designs contained in `selected_design` variable in the following order:

Constraint C4: the script verifies that the maximum stress in the beam, which connects the two rotors, is lower than the admissible stress of the material;

Constraint C5: the vertical equilibrium is considered in order to verify that the total lift (of two rotors) is greater than the total weight (composed by beam, blades of two rotors and two electrical motors weight).

Constraint C6: it verifies that, the maximum stress in the spar caps of the blade is lower than the admissible one.

At the end of this script, other designs contained in `selected_design` variable are removed and two new output variables, `selected_design2` and `rejected_design2` are created. The first output variable is similar to `selected_design` but with more columns and, in general, lower number of lines because of the application of other three constraints. In addition to six variables already mentioned for `selected_design`, other five columns are added resulting in a Lx10 cell variable with L designs where $L \leq N$. So, column 7

contains the mass of the structural beam, while, columns 8 and 9 contains two vectors as in Figure 4.6. In particular, column 8 contains the results of beam strength constraint (C4 in Figure 4.6) while, column 9 the result of the vertical equilibrium constraint (C5 in Figure 4.6) both for each θ angle (angle of attack of the rotor). In both columns, the value 1 is assigned at each angle θ, for a given design, at which the constraint is satisfied while 0 in the other case. Furthermore, the last column holds the blade constraint result (C6 in Figure 4.6) of each design: value 1 means that the blade can bear the aerodynamic flapping moment, otherwise 0 appears. Since the lift force decreases with θ but, decreasing θ, the required wind speed rapidly increases, its not possible to pass both constraint for each θ. For this reason, a lower and upper value of θ are given as input and the aforementioned constraints are checked only for a limited range of rotor angle of attack.

	B	R	Q_e	T	c	P	m_b	C4	C5	C6
	[−]	[m]	[Nm]	[N]	[m]	[kW]	[kg]			
D_1	2	5	500	4500	0.2	14.42	179.85	vector	vector	1
D_2	2	5	500	4500	0.3	11.78	179.85	vector	vector	1
D_3	2	6	500	4500	0.3	9.18	212.55	vector	vector	1
...										
D_L	3	6	500	4500	0.2	9.18	212.55	vector	vector	1

θ[°]	66.8	57.9	49.7	42.6	36.7	31.9	28.0	24.8	22.1	20.0
D_1	1	1	1	1	1	1	1	1	1	1

θ[°]	66.8	57.9	49.7	42.6	36.7	31.9	28.0	24.8	22.1	20.0
D_3	0	0	1	1	1	1	1	1	1	1

Figure 4.6: Example of `selected_design2` variable with an extract of vectors C4 and C5.

The second output variable, `rejected_design2`, is similar to `rejected_design` but with 3 more columns corresponding to the last 3 constraints. This variable is an Mx12 matrix where the first five values on each lines represents the design parameters; the sixth value is the electrical power and the last six columns contain the results of 6 constraints. In

particular, these last six columns contains only 0 or 1: 0 for each passed constraint, 1 for not passed constraint. Since this matrix contains the rejected designs, at least a constraint with 1 on each line is expected. This variable is created in order to keep track of the reason why each design is rejected to suggest improvement in the design.

4.3. Default settings

The simulations carried out contain many free parameters and it is not possible to intervene at the same time on the optimization of all of them. For this reason, some parameters have been set and kept the same for all simulations; in particular it is the case of structural parameters.

First of all, a configuration was chosen consisting of 2 rotors of radius R connected by a beam whose section is depicted in Figure 3.8. The first parameter set was the gap between the rotors (minimum distance between the ends of the blades of the 2 rotors) equal to 1 meter. With this, since the radius of the rotors varies during the analysis, a beam length equal to $\ell = 2\mathrm{R} + 1$ has been set where the rotor shafts are at the ends of this beam. This beam is made of wood and its section, depicted in Figure 3.8, is defined imposing the following dimensions:

- $\mathrm{b} = 0.13\,\mathrm{m}$;
- $\mathrm{h} = 0.32\,\mathrm{m}$;
- $\mathrm{b}_a = 0.04\,\mathrm{m}$;
- $\mathrm{h}_a = 0.22\,\mathrm{m}$.

Furthermore, to link the system to the ground, a cable connected to the beam in 2 points is used as shown in Figure 3.2. The position of these 2 points is imposed and depends on the length of the beam. In particular, the distance a (Figure 3.2) is required to be 20% of $\ell/2$ while the distance d is calculated in such a way to have an angle $\gamma = 50°$.

Finally, the blade parameters are set. The spar caps, with the task of resisting to flapping moments, are made with composite material of unidirectional glass fiber and a triaxial glass fiber shell. The airfoil used is the GOE 429 with a mean drag coefficient $\delta = 0.006$ and a constant airfoil pitch angle $\alpha = 0.035 = 2°$ along the blade span. Moreover, an air density of $\rho = 1.168\,\mathrm{kg/m^3}$ is chosen.

5 | Results

In this section, as already said, the results produced by the script are shown and commented. At the beginning of the process, a parametric analysis is performed in order to explore the space of design variables and to assess the effect of each of them on the produced electrical power. Then, some configuration for different power size (5 kW, 30 kW and 100 kW) are extracted and analyzed in more detail.

5.1. Simulation settings

First of all, the simulation must be set by choosing the values of the various inputs described in 4.2.1. First of all, the operating altitude must be chosen in order to use the corresponding air density. Then the airfoil of the blades must be chosen from which the average drag coefficient is calculated. Finally, the 5 vectors, used for the parametric analysis, containing the number of blades B, the chord c, the radius of the rotor R, the electric torque Q_e and the thrust T must be defined. Since most AWE systems are designed to operate at altitudes below 1 km [25], an altitude of 500 m was considered in this analysis to be able to compare the results with other AWE systems. For this reason, an air density of $\rho = 1.168\,kg/m^3$ which, from the standard atmosphere model, corresponds to an altitude of 500 m is set. Than, following the simulation developed in [6], the GOE 429 airfoil with an average drag coefficient of $\delta = 0.006$, is used for the blades since it is widespread in autogyros applications. For the others design parameters, the values in table 4.1 are used as starting point to define the input vectors as follows:

- number of blades B = [2 3 4];
- blade chord c = [0.2 : 0.05 : 0.8] m;
- rotor radius R = [3 : 0.3 : 8.1] m;
- electrical torque Q_e = [100 : 200 : 3100] Nm;
- thrust T = [1000 : 300 : 6100] N.

5.2. Global results

With this simulation about 200 thousand designs of a **single rotor** were analyzed and used in order to produce Figures 5.1, 5.2 and 5.3.

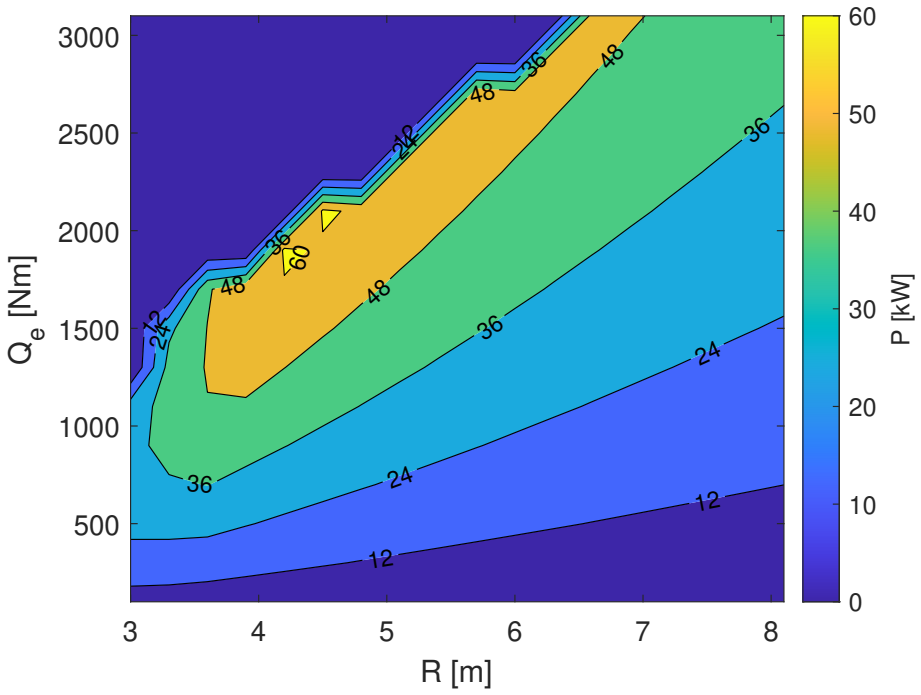

Figure 5.1: Electrical power P of single rotor with respect to the rotor radius R and electrical torque Q_e.

These figures are obtained starting from the whole data obtained and plotting, for each combination of two variables (R and Q_e, R and T, R and c), the maximum value of electrical power that can be produced among the designs that have in common these two selected variables.

In Figure 5.1 it is shown the maximum power with respect the torque and the blade radius. In particular, each point in this plot represents the maximum electrical power among all the designs, with different thrust T, chord c and number of blades, but the same combination of Q_e and R. It is important to underline that, in order to produce these plots, the first three constraint have already been applied to remove the nonphysical design. In particular, in addition to the model constraints, also the minimum wind speed for steady state operation is introduced. If not, too high power designs would be produced (they would have required too high wind speed) distorting the analysis results. This is the reason why this graph presents a zero-power region: this region, in fact, represents a

combination of variables that produces rejected designs. From this graph it is also noted that the maximum power is produced for torque values higher than 1000 Nm and that this value increases as the radius of the rotor increases.

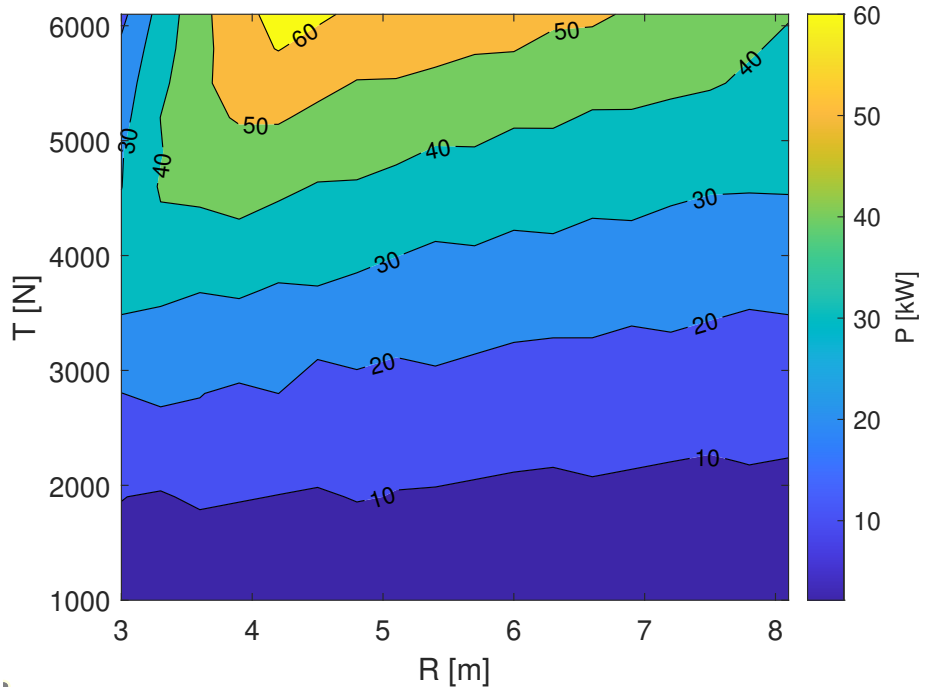

Figure 5.2: Electrical power P of single rotor with respect to the rotor radius R and thrust T.

The same procedure just described was used to obtain Figure 5.2 as well. Here, the influence of the rotor radius and thrust on the output power for a single rotor is assessed. This figure explains that the power produced increases with the thrust generated and that, once the power is fixed, the increase in the radius requires an increase in thrust.

This does not mean that smaller radius designs are the best: always remember that each design has different wind speed values required to operate in steady state. It will be shown later that, although on one hand bigger radius reduces the power produced, on the other hand it reduces the required wind speed. This allows operation even in less windy areas or, in any case, extends the operating time.

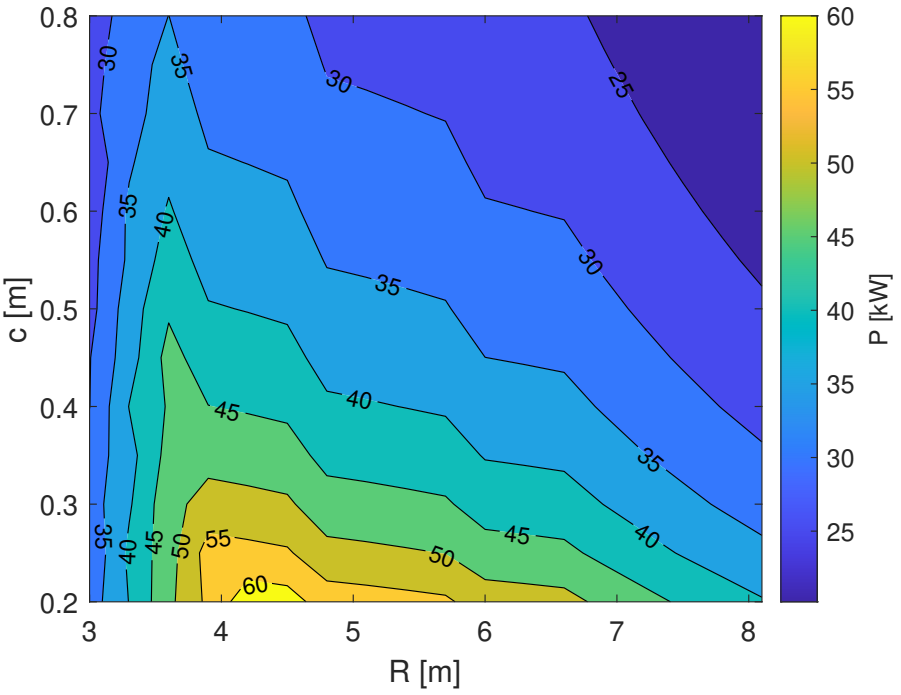

Figure 5.3: Electrical power P of single rotor with respect to rotor radius R and blade chord c.

Finally, Figure 5.3 presents the influence of the radius and chord of the blade on the electrical power. It shows that lower values of the blade chord lead to low electrical power design and that, for fixed power, an increase in rotor radius requires a smaller chord.

The first part of the analysis made it possible to obtain general information regarding the production of power by means of autorotating rotors. In fact, it has made possible to evaluate the effects of the design variables on the electrical power. Now it is necessary to consider particular aspect of the considered autorotational AWE system. The AWE system in question is composed by two, equal and counter-rotating rotors connected by a beam. In turn, the beam is connected in 2 points (distance a from the beam ends) with a cable that binds it to the ground. The choice of using 2 counter-rotating rotors was taken to obtain a zero resulting torque and to avoid a continuous twisting of the cable that could break it. Having said this, it is possible to move on applying the other 3 constraints (see 4.2.2) and get designs with different power sizes. In the following, 5 kW 30 kW and 100 kW designs are extracted and analyzed in further details. But before, another analysis involving a single design is performed.

5.2.1. Perturbation of a fixed design parameters

The global analysis is used as first method to understand the effects of design variables on the output electrical power. In addition to this, a further analysis is performed on a single design in which the parameters are perturbed. The aforementioned design is the D2 design which will be discussed later.

The plots showing the influence of rotor radius R, electrical torque Q_e, thrust T and chord c, on the power produced and on wind speed for steady state operation, will be shown and commented. In Figure 5.4 the effect of increasing the rotor radius are depicted from two point of view: the variation in electrical power and the required wind speed. From this figures, can be noticed that, an increase in the radius produces a decrease in power production. This, doesn't mean that small rotor are better; in fact, this lower power is due to the lower wind speed required. So the advantage of increasing the radius, is that energy can be produced from lower wind speed.

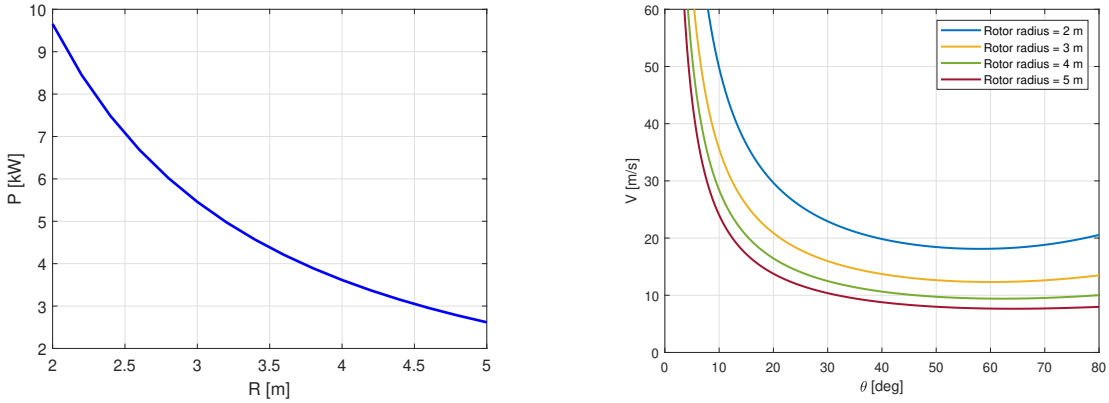

(a) (b)

Figure 5.4: Electrical power trend as function of rotor radius R (a). Trend of wind speed, as function of rotor angle of attack θ, parameterized over the radius R (b).

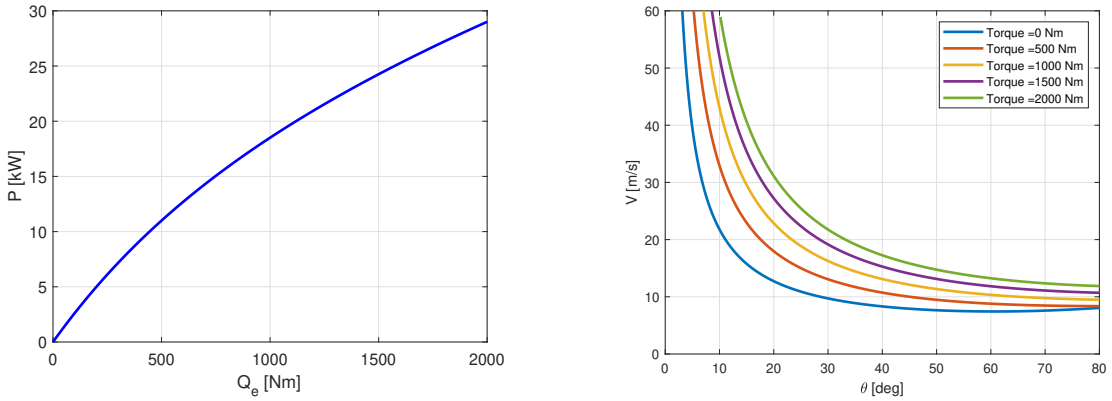

(a) (b)

Figure 5.5: Electrical power trend as function of electrical torque Q_e (a). Trend of wind speed, as function of rotor angle of attack θ, parameterized over the electrical torque Q_e (b).

In Figure 5.5 the effects of electrical torque Q_e over P and V as function of θ are shown. Unlike the previous case, it emerges that a power increase is found as a consequence of electrical torque rise. On the other hand, greater torque applied to the rotor shaft reduces its angular velocity requiring higher wind speed compared to the perfect autorotation ($Q_e = 0$). The effects of the thrust are depicted in Figure 5.6 where, an increase in this parameter induces an electrical power and required wind speed growth.

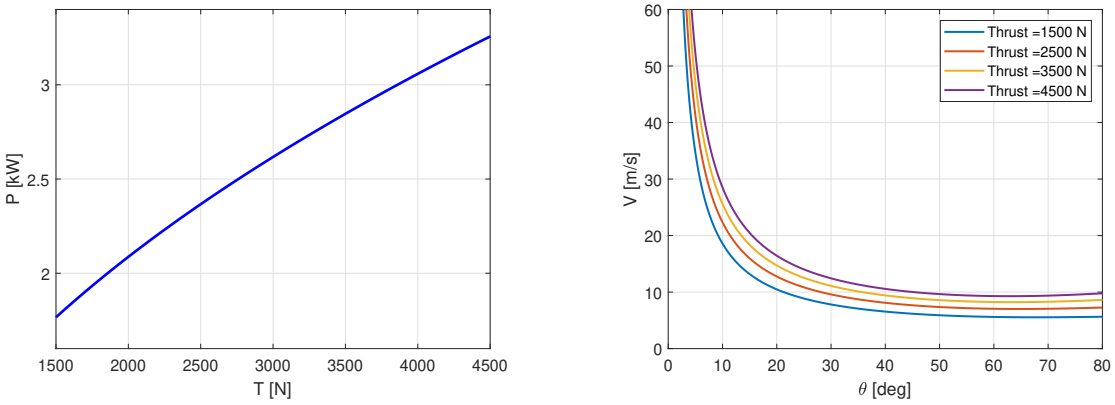

(a) Effects on P. (b) Effects on V.

Figure 5.6: Electrical power trend as function of thrust T (a). Trend of wind speed, as function of rotor angle of attack θ, parameterized over the thrust T (b).

Finally, in Figure 5.7 can be noticed that an increase in the blade chord led to a lower

energy production but now, the required wind speed reduction is not as significant as in the previous cases.

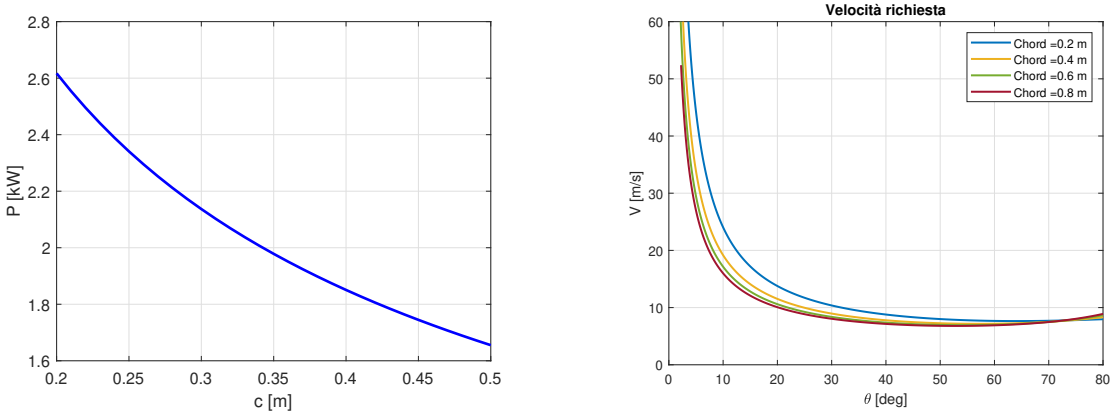

(a) Effects on P.

(b) Effects on V.

Figure 5.7: Electrical power trend as function of chord c (a). Trend of wind speed, as function of rotor angle of attack θ, parameterized over the chord c (b).

In conclusion, this analysis has provided further information regarding the influence of the various parameters on the system performance. From here, it is also clear that it isn't correct to consider only the electrical power produced but it is also essential to consider the required wind speed. Otherwise it would tend to produce configurations which theoretically could produce a lot of energy but which in practice would not work due to the absence of the adequate wind speed.

5.3. Particular configurations results

Before moving on to the actual results, it is useful to make a premise about what will be shown. The iterative method described in [6], although proposed for the AWE world, does not allow to carry out a typical wind energy project. In this field, in fact, the nominal power to be produced is an input and consequently the design variables are determined to produce this power. The method used in this thesis, on the other hand, is based on the definition of all the project variables and a consequent calculation of the electrical power which is an output. All of this serves to justify the fact that the designs shown will not exactly reach 5 kW but will be close.

5.3.1. 5 kW configurations

After this premise, 3 designs are shown and analyzed in detail to better understand the effects of some parameters just mentioned. These three configuration of about 5 kW in total (power of two rotors) are shown in Table 5.1 with their design variables.

	B [-]	R [m]	Q_e [Nm]	T [N]	c [m]	P_{tot} [kW]	V(20°) [m/s]	V(40°) [m/s]	θ_{max} [deg]	$V_{\theta_{max}}$ [m/s]	Ω [$\frac{rad}{s}$]	W_{tot} [N]
D_1	2	4	100	3000	0.3	**5.90**	14.8	9.9	43	9.8	29.5	1909
D_2	2	5	100	3000	0.2	**5.23**	13.8	8.8	41	8.7	26.2	2157
D_3	2	5	100	4000	0.3	**4.99**	14.0	9.3	45	8.9	25.0	2546

Table 5.1: Designs of about 5 kW.

In this phase, the speed required to operate in steady state conditions was considered in more detail. In particular, the wind speed required to operate at 20° and 40° is shown, where 20° and 40° represent the imposed extreme of the angle θ during operation. In practice the last three constraints have been applied in that interval since they cannot be satisfied for every θ, so, a restricted interval is chosen for design procedure. In addition, the θ_{max} angle has also been introduced which represents the maximum incidence of the rotors (θ) for which the constraints are satisfied then, the corresponding wind speed ($V_{\theta_{max}}$) has also been calculated. This speed represents the minimum for steady state operation for a certain design.

The comparison between the required wind speed for each design is shown in Figure 5.8. It can be noted that V decreases with the angle of attack of the rotors but after a certain angle, the vertical equilibrium ceases to be verified. For this reason, the working angle θ and its corresponding wind speed are a fundamental parameter because the vertical equilibrium must be satisfied while the required wind speed should be low in order to maximize the energy production time. Now, from Figure 5.8 the **Design 2** is chosen because, at almost the same power production, it requires the lowest wind speed.

Finally, it was decided to further improve this design to increase the θ_{max} angle which, in turn, reduces the minimum wind speed required for steady state operation. By checking the vectors corresponding to the constraints C4 (structural constraint) and C5 (vertical equilibrium) in Figure 4.6 it was found that the structural one was always verified while the limiting one was the lifting constraint. With this, a modification of the beam section was carried out to lighten it and extend the θ interval for which the vertical equilibrium is satisfied. So, by changing the parameters of the beam section depicted in Figure 3.8 as

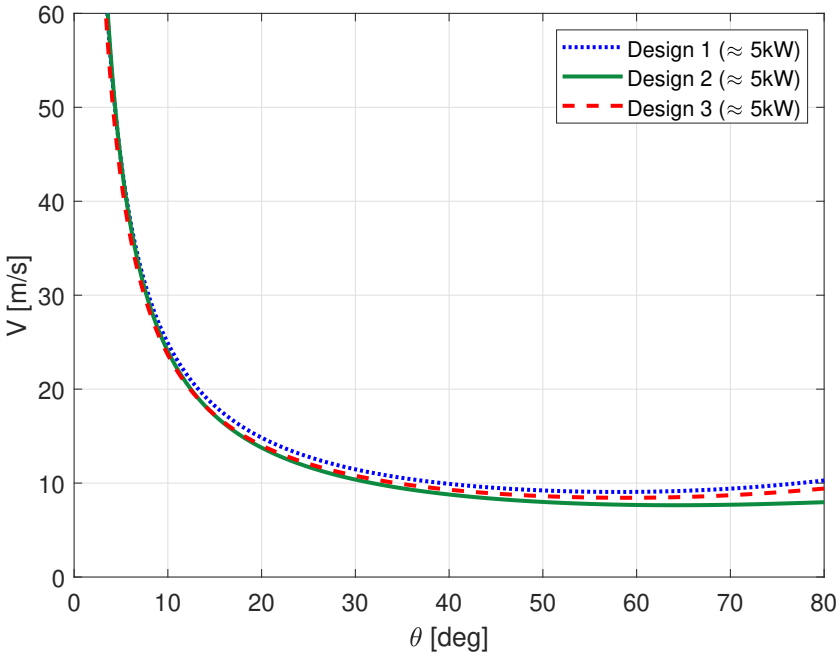

Figure 5.8: Comparison of required wind speed for design D_1, D_2 and D_3.

follows:

- $b = 0.13\,m$;
- $h = 0.26\,m$;
- $b_a = 0.04\,m$;
- $h_a = 0.2\,m$.

a θ_{max} of 49.32° is obtained with a corresponding wind speed $V_{\theta_{max}} = 8.0\,m/s$ and a total weight $W_{tot} = 1672\,N$. In the end, a small variation in the beam section has produced an improvement in the system performance and a reduction of its cost. Now, in fact, it can operate at higher angles of attack allowing energy production from lower wind speed with also a lower cost due to the reduction of material.

5.3.2. 30 kW configurations

The premise made in 5.3.1 also applies to designs of about 30 kW, in fact only designs in the vicinity of this rated power are obtained. The selected design, that has passed all the six constraints are listed in Table 5.2. For this power size, it can be noted that the thrust and the rotor radius are similar to those of the 5 kW case, while, there has been an increase in the electric torque required and in the wind speed to operate in steady state.

	B [-]	R [m]	Q_e [Nm]	T [N]	c [m]	P_{tot} [kW]	V(20°) [m/s]	V(40°) [m/s]	θ_{max} [deg]	$V_{\theta_{max}}$ [m/s]	Ω [$\frac{rad}{s}$]	W_{tot} [N]
D_4	2	4	500	3000	0.2	**29.31**	22.1	13.3	47	12.1	29.3	1852
D_5	2	5	600	3800	0.2	**30.02**	20.0	11.9	53	10.3	25.0	2254
D_6	2	4	500	3500	0.2	**32.74**	22.9	13.8	56	11.7	32.7	1865
D_7	2	4	500	4000	0.3	**32.74**	20.6	13.0	59	11.3	29.3	2001

Table 5.2: Designs of about 30 kW.

Comparing the plots of required wind speed as a function of the θ angle, as depicted in Figure 5.9, it can be seen that the D_4, D_6 and D_7 designs have a very similar behavior while, the D_5 design requires a lower speed.

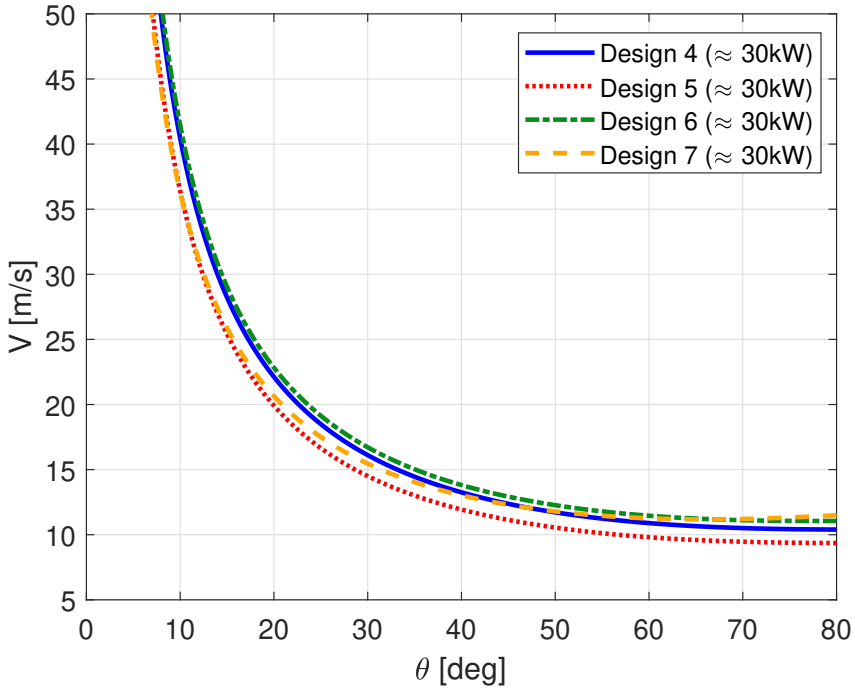

Figure 5.9: Comparison of required wind speed for design D_4, D_5, D_6 and D_7.

In particular it requires a minimum wind speed, at angle θ_{max}, lower than others designs of at least 1 m/s. This particular behaviour is due to the higher radius of this design with respect to the others. In fact, a grater rotor radius, at fixed power, requires lower wind speed but, on the other hand the blade flapping moment will increase. Following that, the design D_5 is suggested for production of about 30 kW even tough it wasn't possible to further lighten the structure to increase the θ_{max} angle and further reduce the minimum

operating speed.

5.3.3. 100 kW configurations

At the end of the analyses, also the 100 kW designs are studied for which some problems were encountered. In fact, after the first analysis carried out with the parameters already described, no 100 kW design had passed all 6 constraints although there were designs with even higher power. So, after these results, it was decided to understand the cause by analyzing the `rejected_design2` variable which indicates all the constraints not passed by each design. Therefore, 63 designs, which had passed the first 3 constraints, with power between 49 and 51 kW were considered. Constraints 4, 5 and 6 were also analyzed, obtaining the following results:

Constraint 4: 100% of the designs did not pass constraint 4. It means that in all 63 cases, the structure would have broken due to the applied loads;

Constraint 5: all the 63 designs passed constraint 5 about the vertical equilibrium;

Constraint 6: 51% of the designs, did non pass the blade structural constraint. It means that, in the 51% of the 63 designs, the blade would have broken.

These results can be understood, considering the power to be produced. In fact, it is noted that, to reach 100 kW, the torque and thrust required increases a lot and this stresses the structure more (both beam and blades) while there is a benefit on constraint 5 (vertical equilibrium), given that, the increase in thrust allows you to keep a greater weight in flight. In addition, breaking of the blades is noted in all cases with rotors that have a radius greater than or equal to 5 meters because, in these cases, the bending moment is greater.

After this analysis, it was decided to modify the beam structure since it was linked to the most problematic constraint. First of all, the section of the beam was modified but, to satisfy constraint 4 (beam resistance), its weight increased to such an extent that the vertical equilibrium was no longer satisfied except for extremely small θ angles for which it was required too high wind speed. So it was decided to change the material: from wood to aluminum 6082. With this new material, the beam section was reduced as follows:

- $b = 0.06\,m$;
- $h = 0.1\,m$;
- $b_a = 0.01\,m$;
- $h_a = 0.08\,m$.

and different designs, that passed all the 6 constraints, are found. Some of them are listed in Table 5.3. In Figure 5.10 is shown the minimum wind speed required to operate in steady state for each design. It should be noted that design 10, with 4.5 m rotor radius, and the design 11 with 3 blades require slightly lower speeds than the other two. In particular, design 10 is the one that allows for the lowest required speed. This was predictable given that it has a rotor radius of 0.5 m higher than the others and therefore manages to harvest wind energy over a greater surface. At the end, for what has just been said, the design D_{10} is suggested for production of 100 kW of electrical power.

	B	R	Q_e	T	c	P_{tot}	V(20°)	V(40°)	θ_{max}	$V_{\theta_{max}}$	Ω	W_{tot}
	[-]	[m]	[Nm]	[N]	[m]	[kW]	[m/s]	[m/s]	[deg]	[m/s]	$[\frac{rad}{s}]$	[N]
D_8	2	4	1800	4500	0.2	**99.64**	37.8	21.4	74	15.6	27.7	1161
D_9	2	4	1500	5200	0.2	**99.70**	35.4	20.5	75	15.2	31.3	1161
D_{10}	2	4.5	1900	5100	0.2	**100.22**	34.6	19.7	71	14.6	26.4	1256
D_{11}	3	4	1800	5800	0.2	**100.78**	32.9	19.43	73	15.0	28.0	1312

Table 5.3: Designs of about 100 kW.

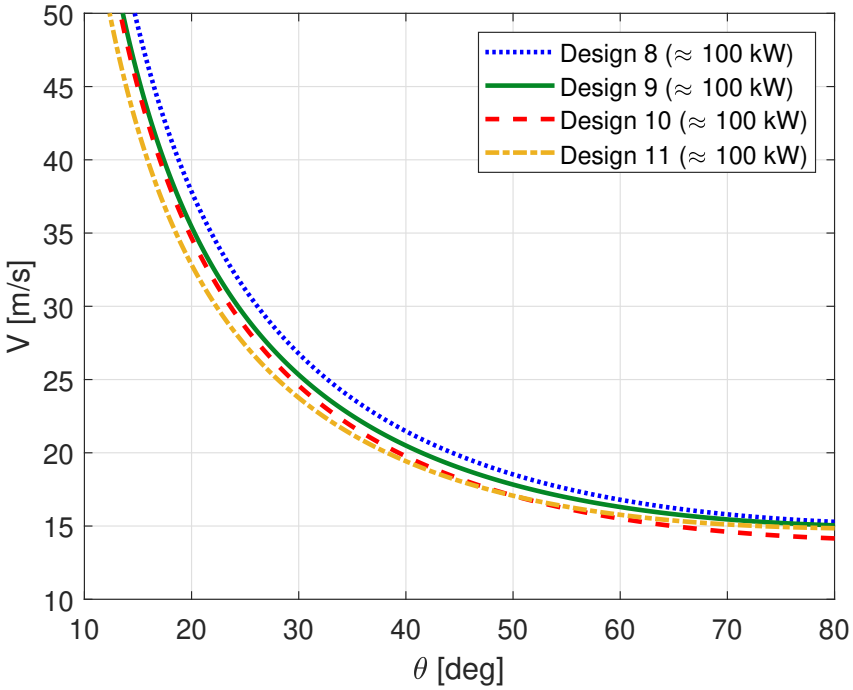

Figure 5.10: Comparison of required wind speed for design D_8, D_9, D_{10} and D_{11}.

6 | Conclusions

In this thesis, an analysis of an autorotational AWE system was performed with the aim of obtaining an estimate of weight and size of the rotors for three configurations of different power. At the end of the analysis, the aim of the thesis is achieved although some problems, related to the several hypotheses introduced, were encountered. These problems encountered, however, provided the opportunity to identify the major criticalities of the models used. It is precisely this analysis, which subsequently led to the formulation of possible improvements described in future developments.

In the first chapter the AWE world was briefly introduced and then the autorotation principle, with its possible applications for wind energy harvesting, is discussed. Subsequently, the mathematical model of autorotation developed by Glauert [12] and used by Rimkus and Das [6] was exposed. The notable simplifications were explained and subsequently the structural model was developed. After that, the Matlab script was developed and the first results were obtained. From the global analysis it can be deduced that the maximum power of a single rotor is produced using rotors with radius between 4 and 5 m with 2 blades of constant airfoil chord of 0.2 m. Morover, an electrical torque Q_e around 1500 Nm and a thrust between 5000 and 6000 N are required. However, these results are already those that have passed the first 3 constraints and in this passage, many designs have been discarded. From the analysis of the `rejected_design` variable, it was possible to identify the most critical constraints. In particular, approximately 202 000 design are considered and only 96 096 passed the first three constraints. Considering the rejected 106080 designs, it emerged that:

Constraint 1: 0% of the rejected design has been removed because of this constraint. In fact, also in [6] they say that this last constraint isn't too restrictive.

Constraint 2: 99.2% of rejected designs cannot satisfy constraint 2 because of the stall of some blade elements;

Constraint 3: 6.2 % of rejected designs cannot satisfy constraint 1 because they require a minimum wind speed for operation which is higher than the 16 m/s imposed;

It is worth pointing out that the sum of the percentages is not 100. This is due to the fact that, some discarded designs do not satisfy both constraint 1 and constraint 2. These results underline how stringent the constraint 2, related to the stall of the blade element, is and consequently, it also represents the first aspect on which to intervene to maximize the improvement of the autorotational AWE.

Proceeding also with the second phase of the analysis, it was noticed that many designs were discarded due to the last 3 constraints. In particular, for low powers (5 kW) associated with low thrusts T, problems have been found in passing constraint 5 regarding vertical equilibrium. As regards the high powers (100 kW), on the other hand, the required thrust is high and the vertical balance is always verified. However, there are problems related to the resistance of the structure and the blades for which the radius of the rotor does not exceed 4.5 m in radius. For this reason all designs have rotors with a radius between 4 and 5 meters although, in 5.2.1 it was seen that the increase in the radius allows the lowering of the wind speed required for steady state operation.

Among the designs shown in 5.3, the minimum wind speed required is 8.0 m/s (for the 5 kW modified design) while the maximum is 15.6 m/s for the 100 kW design. These are values in line with the speeds that can be found at 500 m altitude as described in [31]. For example in the U.S. Great Plains (in the middle of north America) has an average wind speed of around 15 m/s at an altitude of around 500 m in the summer. Even better, in Somalia and throughout the Horn of Africa, winds above 20 m/s can be found already at altitudes between 500 and 1000 m with power densities greater than 10 kW/m^2. Unlike the Great Plains area, in the Horn of Africa these speeds occur in both summer and winter. Furthermore, near the poles there are the maximum wind power densities that reach 12 kW/m^2. In particular, on the coasts of Greenland, in winter, speeds of just over 20 m/s are reached at altitudes even below 500 m while, in the summer (July), the intensity of the winds drops slightly below 20 m/s. In this period (July), on the contrary, winds slightly higher than 20 m/s are found at altitudes even lower than 500 m along the coast of Antarctica[31].

Finally, after obtaining the designs for 5, 30 and 100 kW it is possible to discuss the results obtained by comparing them with other AWE systems available. The powers produced by the three designs obtained are comparable with those of crosswind AWE technologies, more studied than those based on autorotation. In particular, the *Kitemill* company produces the KM1, a rigid wing and cross-wind AWE system which, following the tests in 2022, showed an average power production of 5.5 kW [2] although, with an optimization on the trajectory and reel-in procedure, it is expected to produce 20 kW. The same company is also working on a larger model, the KM2, with the aim of producing up to 100 kW of power

[3]. Unfortunately no weight data are available about these two models for comparison. The *Skypull* company has designed a different cross-wind system based on 2 wings with multi-element profiles to maximize lift and maintain a small wingspan. Using two wings of 3.2 m , this technology allows to produce up to 25 kW of power. Also in this case, no weight data are available. Finally, the *SkySails Power* company realizes the SKS PN-14 model capable of producing a power between 80 and 200 kW depending on the zones, using a kite (therefore crosswind AWE with flexible wings) with a surface between 90 and 180 m^2 [32]. The 100 kW configuration obtained in this thesis (subsection 5.3.3) is comparable to this AWE system in terms of power and is equipped with a total rotor surface (two rotors) of approximately 127 m^2 (R = 4.5 m). This studied configuration has a mass of about 128 kg which includes the structure, the blades and the generators. The SKS PN-14 model has a kite with a mass of about 50 kg [5] but, to perform an even comparison, to this value must be added the weight of the generator and of the winch on the ground and the mast that reaches a height of 20 meters, for take-off and landing. These additional elements increase the overall weight of the SkySails system. In fact, also the winch in continuous rotation, will be subjected to greater stress and must have a more robust and heavier structure than that of the autorotational AWE studied in this thesis (see 5.3.3). Here it is difficult to evaluate the weight of these components but it is reasonable to assume that the two solutions can have comparable mass and consequently costs of the same order of magnitude. This result, although very approximate due to the limited data available, demonstrates that the autorotational AWE has all the characteristics to be a technology with the chance to compete with the most studied cross-wind systems.

6.1. Future developments

As just seen, the most stringent constraints were that relating to the stall of the blades, the resistance of the structure and the blades. For this reason, possible improvements have been thought to be introduced to solve these limitations and obtain increasingly competitive configurations.

1. As regards the resistance of the structure, 2 possible solutions are proposed.

   1.1. The first solution, also used for the 100 kW design, is to use materials with higher performance although this leads to an increase in cost. This aspect, however, is also justified by the significant increase in power produced compared to the 5 and 30 kW configurations with structure made of wood (less expensive).

   1.2. The second solution is to change the configuration of the cable attachment. Instead of using a single cable, it is possible to use two of smaller diameters

(therefore with a similar weight) connected to the ends of the beam. In this way, the beam can be lightened and modified to withstand only the counter-rotating torques of the 2 generators without having to bear the bending as well. Also, since this system does not move in relative motion, adding a cable does not produce an increase in drag that reduces performance as in cross-wind methods.

2. The blade stall constraint causes about 50% of design eliminations. This is due to the simplifying hypothesis, at the base of the aerodynamic model, of straight blade without twist. In fact, for high rotor radius, stall occurs already in the middle of the blade and this is not admissible. For this reason, it is proposed to implement, in the aerodynamic model, the possibility of inserting a blade twist. In this case it is possible to determine an optimal twist of the blade to make each section work at maximum efficiency with a consequent increase in performance. Furthermore, this modification would allow to solve this problem by allowing simulation with larger rotors that can operate with wind speeds even lower than those found.

3. Another problem encountered concerns the breaking of the blades. This problem was found for high powers which required large rotors and high thrusts. In this case, using a hollow blade section as in Figure 3.9 and using high rotor radius, the blade could not withstand bending. In fact, the structural model used was developed for wind turbine blades with thick profiles near the root. For this application it is therefore proposed to implement the following two solutions.

   3.1. Use airfoils of different thicknesses along the blade starting with thicker profiles near the root. Therefore, the possibility of using different profiles along the blade could be implemented in the aerodynamic model;

   3.2. Modify the blade section using thin airfoil but with internal structure similar to those used in the helicopter field. Also for larger rotors, higher performing materials such as carbon fiber can be used. Although they cost more than fiberglass, the ability to produce much higher power can justify this cost increase.

Furthermore, another problem, already mentioned in 5.3 affected all the results. In fact, the implemented model provides the power produced as an output. In the wind energy field, however, this is not the correct procedure as a system is designed by determining all the parameters in order to produce the nominal power set as input. To adapt the model to such applications, it is therefore proposed to invert the equations used in order to transform the power and wind speed as inputs and to determine the other free parameters

as outputs.

At the end of this analysis it can be concluded that, the autorotational AWE has all the characteristics to become a competitive technology compared to other AWE systems and classic wind turbines, although, a lot of work is still required. As seen in 1.3 this technology has four advantages that allow you to capture high altitude winds with a greater power density but also to modify the operating altitude to maximize the power produced. Therefore it is able to solve two of the typical problems related to the classic wind turbines with horizontal axis. In addition to this, it has been seen that, while using a very simple structure and models, up to 100 kW of electrical power can be produced. More advanced studies, which will allow to introduce the proposed improvements, will increase the size and consequently also the power. Furthermore, a structural sizing to use these systems at even greater altitudes, will make it possible to exploit the large amount of energy contained in the jet streams at altitudes between 7 km and 16 km [13] although you can have effects of power density increasing starting from 5 km [25]. All these possibilities make the autorotational AWE an excellent system on which to invest in research and which, being still in the preliminary phase, still promises considerable improvements.

Bibliography

[1] B. W. Roberts and J. Blackler. Various systems for generation of electricity using upper atmospheric winds. *Proceedings of 2nd Wind Energy Innovative Systems*, pages 67–80, 1980.

[2] Kitemill. Energy produced during testing, . URL `https://www.kitemill.com/news/energy-produced-during-testing`. Accessed on 2022-07-05.

[3] Kitemill. Kitemill projects, . URL `https://www.kitemill.com/projects`. Accessed on 2022-07-05.

[4] Skypull. The skypull technology. URL `https://www.skypull.technology/solution`. Accessed on 2022-07-05.

[5] SkySails. Skysails energy production, . URL `https://skysails-power.com/faq/`. Accessed on 2022-07-05.

[6] Sigitas Rimkus and Tuhin Das. An application of the autogyro theory to airborne wind energy extraction. *Proceedings of ASME 2013 Dynamic Systems and Control Conference*, pages 1–8, 2013.

[7] Airborne Wind Europe. About airborne wind energy, 2022. URL `https://airbornewindeurope.org/about-airborne-wind-energy/`. Accessed on 2022-05-28.

[8] Antonello Cherubini, Andrea Papini, Rocco Vertechy, and Marco Fontana. Airborne wind energy systems: A review of the technologies. *Renewable and Sustainable Energy Reviews*, 51:1461–1476, 2015.

[9] Miles L. Loyd. Crosswind kite power. *Journal of Energy*, pages 106–111, 1980.

[10] Roland Schmehl. Airborne Wind Energy, an introduction to an emerging technology, 2019. URL `http://awesco.eu/awe-explained/`.

[11] Philip Bechtle, Mark Schelbergen, Roland Schmehl, Udo Zillmann, and Simon What-

son. Airborne wind energy resource analysis. *Renewable energy*, pages 1103 – 1116, 2019.

[12] H. Glauert. A general theory of the autogyro. *Reports and memoranda No. 1111*, pages 558–593, 1926.

[13] Cristina L. Archer and Ken Caldeira. Global assessment of high-altitude wind power. *Energies*, 2(2):307–319, 2009.

[14] S. Arya. *Introduction to micrometeorology*. Academic Press: New York, NY, USA, 1988.

[15] Kate Marvel, Ben Kravitz, and Ken Caldeira. Geophysical limits to global wind power. *Nature Climate Change*, 2013.

[16] Sky WindPower website. About airborne wind energy, 2018. URL `https://www.skywindpower.com/`. Accessed on 2022-06-01.

[17] J. Gordon Leishman. Development of the autogiro: A technical perspective. *Journal of Aircraft*, 41(4):765–781, 2004.

[18] Juan de la Cierva and D. Rose. Wings of tomorrow: The story of the autogiro. 1931.

[19] Federal Aviation Administration. *Helicopter Flying Handbook*. United States Department of Transportation, Federal Aviation Administration, Airman Testing Branch, P.O. Box 25082, Oklahoma City, OK 73125, 2 edition, 2019.

[20] J. G. Leishman. *Principles of Helicopter Aerodynamics*. Cambridge University Press, 2000.

[21] B. W. Roberts, D. H. Shepard, Ken Caldeira, M. E. Cannon, David Eccles, A. J. Grenier, and J. Freidin. Harnessing high-altitude wind power. *IEEE Transaction on Energy Conversion*, 22(1):136–144, 2007.

[22] B. W. Roberts and D. H. Shepard. Unmanned rotorcraft to generate electricity using upper atmospheric winds. *Proceedings of 10th Australian International Aerospace Congress*, 2003.

[23] B. W. Roberts. Quad-rotorcraft to harness high altitude wind energy. *Airborne Wind Energy conference, TU Delft*, 2015.

[24] Uwe Ahrens, Moritz Diehl, and Roland Schmehl. *Airborne Wind Energy*. Springer, 2013.

[25] Sadaf Mackertich and Tuhin Das. A quantitative energy and systems analysis framework for airborne wind energy conversion using autorotation. *American Control Conference*, pages 4996–5001, 2016.

[26] M. Garcia-Sanz and Houpis C. H. *Wind Energy Systems: Control Engineering Design*. CRC Press, 2012.

[27] Bilal Salih. An introductory study of the dynamics of autorotatio for wind energy harvesting. Master's thesis, Mechanical and Aerospace Engineering, University of Central Florida, Orlando, Florida, 2014.

[28] J. B. Wheatley. An aerodynamic analysis of the autogiro rotor with a comparison between calculated and experimental results. *National Advisory Committee for Aeronautics*, pages 1–24, 1934.

[29] Elke Bontekoe. How to launch and retrieve a tethered aircraft. Master's thesis, Faculty of Aerospace Engineering, Delft University of Technology, 2010.

[30] PML EV. Specifications of hi-pa drive from pml flightlink ltd. URL `http://www.pmlflightlink.com/motors/hipa_drive.html`. Accessed on 2022-06-18.

[31] Cristina L. Archer, Luca Delle Monache, and Daran L. Rife. Airborne wind energy: Optimal locations variability. *Renewable Energy*, pages 180–186, 2013.

[32] SkySails. Skysails n-class, . URL `https://skysails-power.com/onshore-units/`. Accessed on 2022-07-05.

A | Appendix A

This additional material is introduced with the aim of describing in greater detail the matlab script developed for the study of the AWE autorotational system. In particular, all the functions used will be described in greater detail, including the inputs and outputs. The structure of the developed script is shown in the Figure A.1.

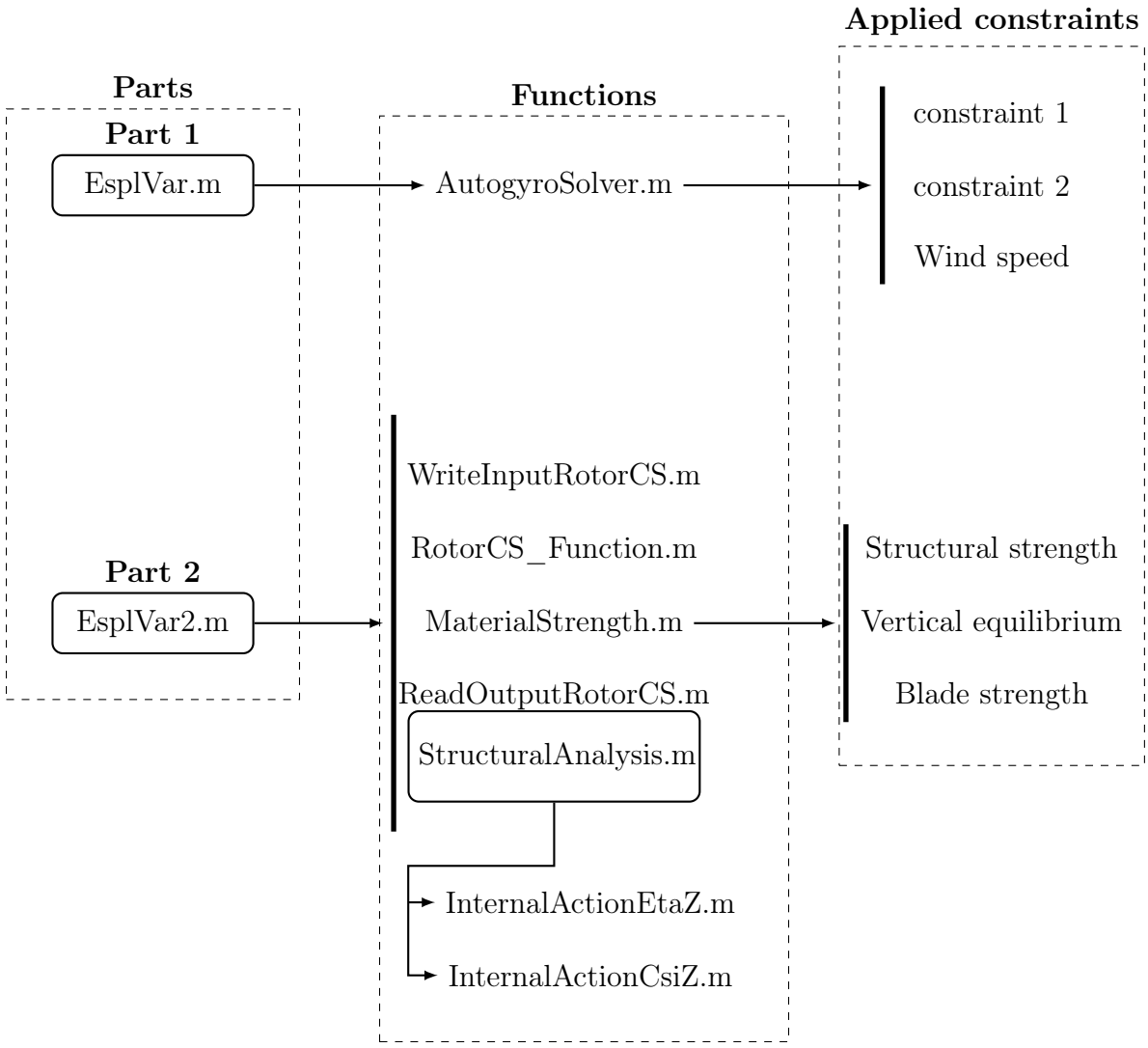

Figure A.1: Structure of the script.

The script used is divided into 2 parts based on 8 functions, which contain the aerodynamic and structural model, and used to apply the 6 constraints considered which will be described again later. The decision to separate the script into 2 parts is linked to two main reasons. The first, and also the most important, is practical as the application of the last three constraints takes more time than the application of the first three. In fact, calculating the blade section with RotorCS is the most time-consuming step of all. For this reason, the constraint application process was divided into two parts in order to avoid solving the blade section even for designs that did not even satisfy the first three constraints. The second reason for the separation into 2 parts is related to the meaning of the constraints considered. In fact, in the first part the designs with physical meaning are selected, i.e. those that satisfy the two conditions imposed by the model and those that require a minimum wind speed that is lower than a certain value `max_Vmin`. On the other hand, the second part considers the constraints linked to the specific design which are the resistance of the structure and the blades and the vertical balance.

A.1. Part 1

Part 1 is contained in the file `EsplVar.m`. This part has the task of defining the inputs used in all simulations and of defining the vectors of the design variables used to carry out the parametric analysis. This analysis is carried out using five nested for loops: one for each of the design variables (B, c, R, Q_e, T) in order to consider all the possible combinations. Subsequently, part 1 allows to apply the following constraints to the created designs (combinations of these five design variables vectors):

Constraint C1: U_T must be positive over the outer half of retreating blades implying that:

$$V_w \cos\theta < \frac{\Omega R}{2} \tag{A.1}$$

Constraint C2: The outer half of the blade operates below the stall angle α_s such that it is required:

$$\alpha_r = \alpha + \phi_r < \alpha_s \qquad \text{for} \quad \frac{1}{2}R \leq r \leq R \quad \forall\psi \in [0, 2\pi] \tag{A.2}$$

Constraint C3: The minimum wind speed required for steady state operation must be lower than an imposed value to avoid designs that requires too high wind speed.

It also allows you to create plots that show the power produced as a function of two design variables as in Figures 5.1, 5.2 and 5.3.

A.1.1. Inputs and outputs

Part 1 defines the inputs common to all simulations and the vectors of the design variables used for the parametric analysis. First, the operating altitude is defined by choosing the air density (`rho` variable), then the aerodynamic profile is chosen which determines the average drag coefficient (`delta`) and the stall angle (`airfoil_stall`). In addition, the pitch angle of each blade section (`alpha`), the maximum wind speed (`max_Vmin`) and the minimum angle of attack of the rotor `theta_min`, at which the system operates, are also chosen. This last input is needed for the application of constraint 2 which must be verified up to the smallest θ angle at which the system operates. Subsequently, the vectors of the design variables are defined by imposing for each of them: minimum value, maximum value and step of variation. In particular, the aforementioned variables are the rotor radius `R`, the chord of the blades `c`, the electric torque `Q_e` and the thrust `T`. The number of blades `B` is not an input because the study is already set up for configurations with 2, 3 and 4 blades.

This first part of the script produces 2 main outputs which are:

1. `selected_design` variable that is a Nx6 matrix where N is the number of designs that have passed the three constraints. Each row of this matrix represents a design and contains, in order, the values of the following quantities: B, R, Q_e, T, c and the electrical power P produced.

2. `rejected_design` variable is a Mx9 matrix where M is the number of rejected designs. The first six parameters of each row are the same used in `selected_design` variable but, in this case, three more columns are added. Each column represents one of the three applied constraints and contains: 1 if a specific design has been rejected because it hasn't passed the constraint that corresponds to that specific column, while, 0 if the design has passed this constraint.

Figure A.2 shows all the inputs and outputs produced by part 1 of the script.

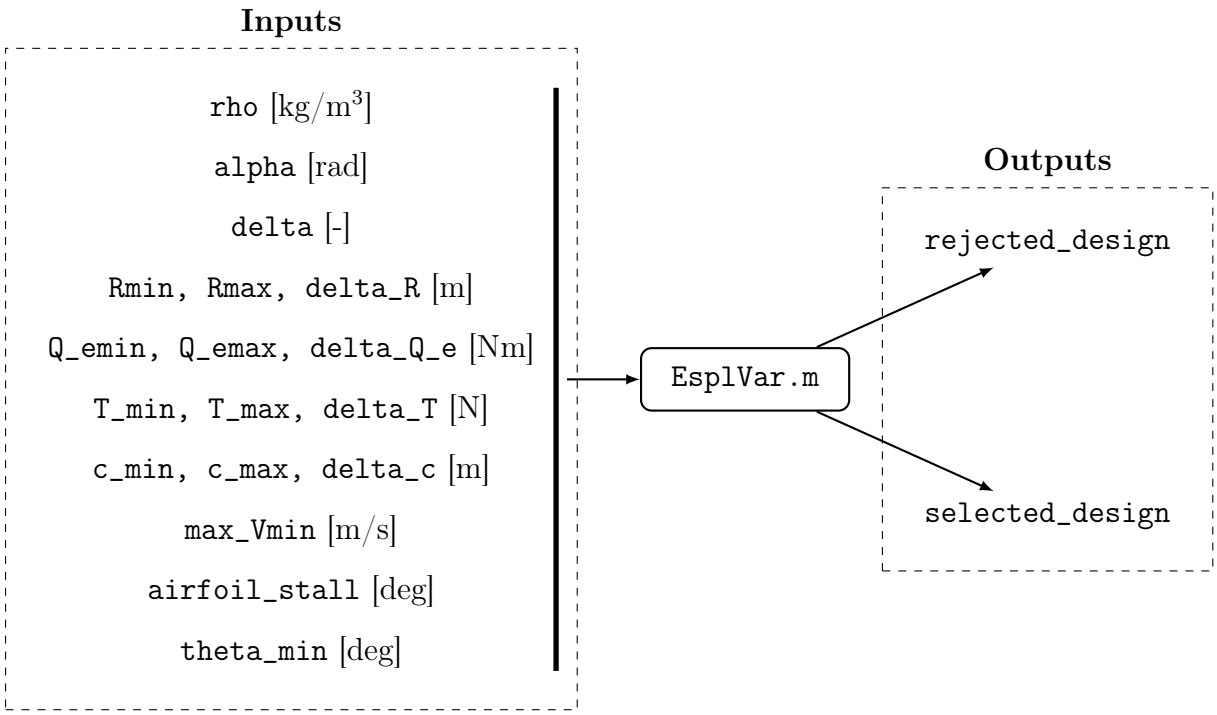

Figure A.2: Input and Output of `EsplVar.m`.

Another important variable is `InputOutput_AutogyroSolver` which contains, for each design that satisfies the first 3 constraints, all the inputs and outputs produced by the `AutogyroSolver.m` function. In fact, this allows to reduce the computational cost and avoid calling the `AutogyroSolver.m` function again in part 2 for the calculation of the lift, drag, θ vector and the wind speed for steady state operation as functio of θ of each configuration.

Finally, the general inputs and outputs variables described are saved in order to be used by part 2 of the script. The `SavePart1.mat` file is thus created.

A.1.2. AutogyroSolver

Part 1 of the script calls only one function: `AutogyroSolver.m`. This function contains the aerodynamic model of autorotation and allows the first evaluation of the parametric analysis designs. Based on the results produced, the first three constraints are then applied. In Figure A.3 the input and output of the `AutogyroSolver.m` function are shown. This function requires as input the air density `rho` at a certain altitude, the blade pitch `alpha` and the mean drag coefficient of the blade airfoil, `delta`. Than it requires the design variables considered in the parametric analysis such as the number of blades `B`, rotor radius `R`, electrical torque `Q_e`, design thrust `W_d` and the airfoil chord `c`.

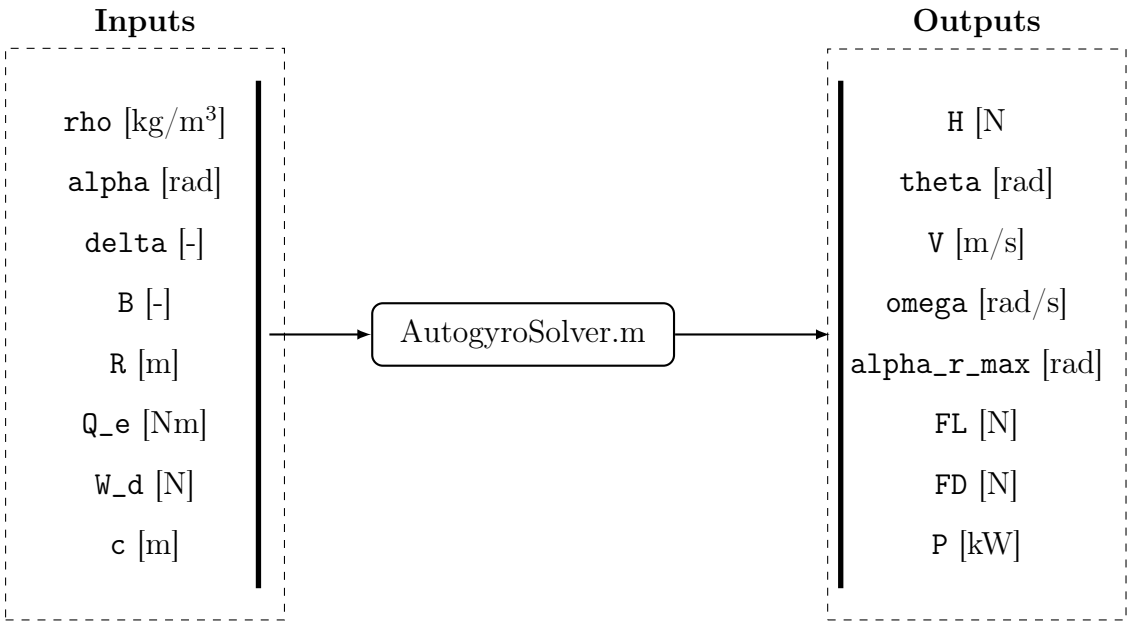

Figure A.3: Inputs and Outputs of `AutogyroSolver.m`.

This function produces as output the longitudinal force on the rotor (`H`) which, with the thrust set as input, makes it possible to calculate the lift `FL` and drag `FD` of the rotor in autorotation. Among the outputs there is the `theta` vector used for the calculation of the aerodynamic loads. It is important to note that all aerodynamic loads such as `H`, `FL` and `FD` are vectors containing the respective force for each angle of the `theta` vector (vector that contains different values of θ). Than the `alpha_r_max` variable represents the maximum value of α_r that is the maximum airfoil angle of attack in the outer half blade. It is used in part 1 to make a comparison with respect the stall angle in constraint 2. Also the `V` variable is used in the application of constraint 1 and constraint 3. This variable is a vector with the required wind speed for each angle θ contained in variable `theta`. Here it can be noted that the vector `theta` is important given that it influences the other variables. In particular, the length of this vector is determined by the choice of the initial guess for the vector τ introduced in 2.3. This vector is not an input and has been set as $\tau = [0 : 0.01 : 0.8]$ so the `H`, `FL`, `FD` and `V` vectors will have 81 elements like τ. Finally, the variable `omega` represents the rotor angular speed Ω, that is used to compute the electrical power P given the electrical torque Q_e set as input.

A.2. Part 2

Part 2 is performed by the Matlab script `EsplVar2.m`. This part has the task of reading the results produced and saved by part 1 and subsequently to apply the following last

three constraints:

Constraint C4: the script verifies that the maximum stress in the beam, which connects the two rotors, is lower than the admissible stress of the material;

Constraint C5: the vertical equilibrium is considered in order to verify that the total lift (of two rotors) is greater than the total weight (composed by beam, blades of two rotors and two electrical motors weight).M

Constraint C6: it verifies that, the maximum stress in the spar caps of the blade is lower than the admissible one.

Part 2 takes all the designs that satisfy the first 3 constraints and, starting from the aerodynamic loads applied to the 2 rotors and known the masses of the various components, allows to calculate the internal actions in the beam that connects the 2 rotors. Consequently, it allows to compare the stresses in the beam with the maximum allowable stress of the material. Subsequently, it calculates the mass of the blades with a geometry defined through the Excel input file (`GOE_429_autogyro.xlsx`) and checks its resistance using `RotorCS`. Once the size of the beam and the structure of the blades are known, it is possible to calculate their mass. Finally, the mass of the generators/motors M_m is calculated from the produced power according to the following simple law $M_m = \mathrm{P[kW]}/2.5[\mathrm{kW/kg}]$ [29, 30]. Once the masses of each component are known, it is possible to calculate mass and total weight. By comparing the lift of the two rotors with the total weight of the structure, it is possible to verify, for which angles of incidence of the rotors, the vertical balance is verified. In fact, it is important to remember that, the variable `FL` is a vector that contains the lift as a function of θ angles and that it decreases with increasing incidence (see Figure 4.2 blue line). Then there is the description of the inputs and outputs of part 2 with the description of all the functions it uses.

A.2.1. Inputs and outputs

As already seen, part 2 carries out the structural analysis of beam and blades and verifies the vertical equilibrium. For this reason, as input, the `b, b_a, h` and `h_a` beam dimensions are required (see Figure 3.8) which define the section of the beam while its length ℓ depends on the size of the rotor, considered each time, according to the following law $\ell = 2\mathrm{R} + 1$ (a minimum distance of one meter between the rotors is maintained). The position of the cable attachment is then defined using the `a_percent` and `gamma` parameters. The `a_percent` parameter represents a value between 0 and 1 that is used to multiply $\ell/2$ (half of beam length) in order to obtain the distance of the cable attachments from the beam ends (a variable). These parameters described in 3.1 are used instead of a

and d to obtain similar designs as the length of the beam changes. As seen in 4.2.2, the vertical equilibrium is not always satisfied for each θ therefore an operating range defined by `theta_min` and `theta_max` is defined. In addition, the hub radius `Rh` is also required which is one of the inputs for RotorCS. Finally, the names and paths of the following files are required as input:

`MaterialFile:` it is a string that contains the path of a .mat file that contains the property of beam material;

`OutputFolder:` it is a string that contains the output folder path of RotorCS;

`InputFilePath:` it is a string that contains the path of the folder in which are collected the different input Excel file for RotorCS;

`ExcelFile:` it is a string that contains the Excel file name used as input for RotorCS. This file must be contained in the folder path that corresponds to `InputFilePath`.

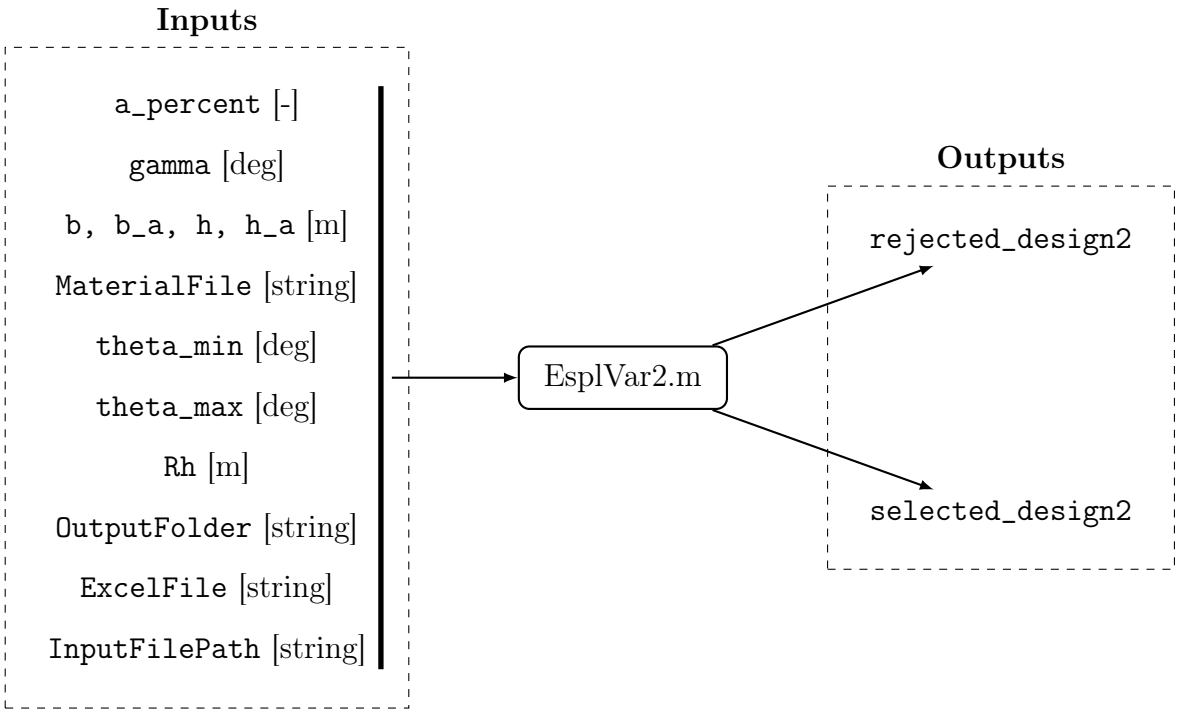

Figure A.4: Inputs and Outputs of `EsplVar2.m`.

A.2.2. WriteInputRotorCS

RotorCS is a program developed by DTU and Politecnico di Milano for the study of the blade section. This program requires all input to be provided via an Excel file. This function then has the task of modifying this file for each of the designs produced during

the parametric analysis. The required input and the output of this function are listed in Figure A.5. This function requires as input the number of blades `B`, the radius `R` of the rotor and the radius of the hub `Rh`, used to define the length of each blade, and the chord of the airfoil `c`. Then it requires the variable `T_thrust` representing rotor thrust, so called, to distinguish it from the shear force introduced in this function. It also requires the `alpha_deg` pitch angle expressed in degrees, the coning angle `beta_0` in radians and, finally, the variable `ExcelFile` containing the name of the excel input file for RotorCS.

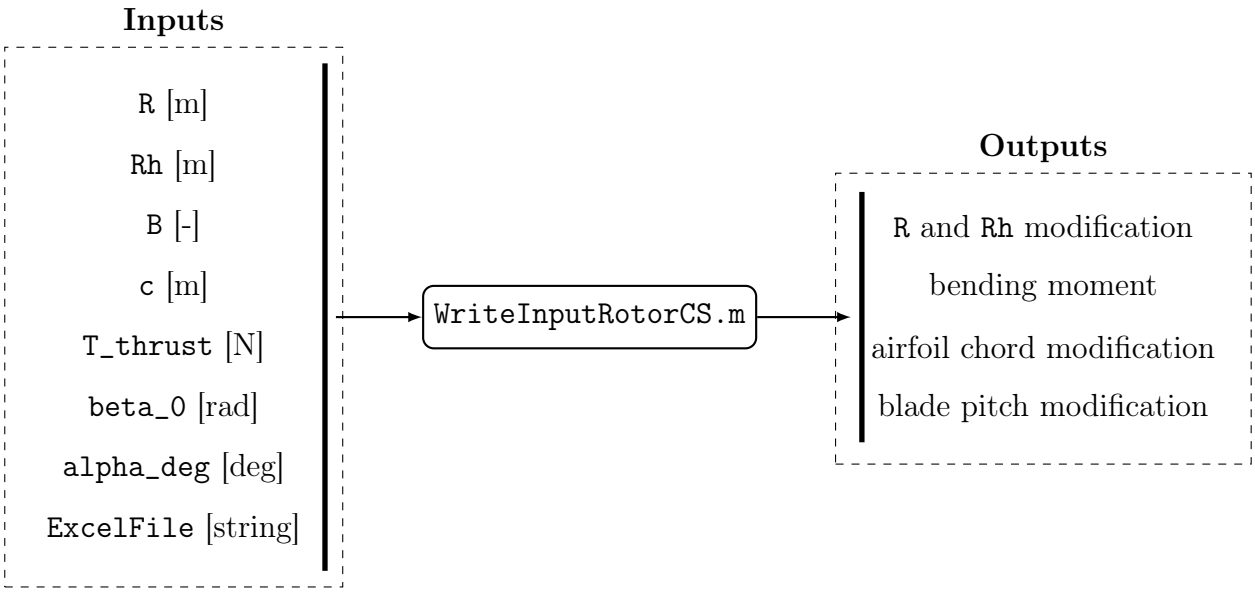

Figure A.5: Inputs and Outputs of `WriteInputRotorCS.m`.

This script has the task of calculating the load on each blade starting from the thrust on the rotor. Then, it determines the flapping moment to be inserted in the "Loads" sheet of the Excel input file. In the Excel sheet called "Settings", the radius of the rotor and the hub is changed, while in the sheet "Blade_Layout" the chord is modified. In this sheet, some changes have been introduced in order to obtain similar sections. In particular, the width of each structural element, seen in the plan that contains the chord and the blade axis, was scaled with the chord. Finally, still in the "Blade_Layout" sheet, it changes the pitch angle of the blade sections by replacing the value of `alpha_deg`.

A.2.3. RotorCS_Function

This function contains exactly RotorCS which reads, as input, the Excel file already seen above. This function was created with the purpose of calling the RotorCS script for each design of the parametric analysis in order to check the blades strength and to compute

their mass. So, this function is used to check the constraint over the blade structure and to compute the blade mass used for the vertical equilibrium constraint.

A.2.4. MaterialStrenght

This function has the task of opening the Excel input file for RotorCS and reading the material used for the blade spar caps. So, it requires only one input that is `ExcelFile` that contains the name of the Excel input file. Than it looks for, within this same file, the tensile and compressive strength of this material. These two outputs are then used in `EsplVar2.m` for the application of constraint 6 about the blade resistance to the aerodynamic loads.

A.2.5. ReadOutputRotorCS

This function has the task of reading the stresses that the aerodynamic loads produce inside the spar caps of the blade. For this reason, it requires as input the path of the folder that contains the output files (`OutputFolder`). Subsequently, the function is able to read the compression and tensile stresses in two spar caps and supply them as output to the `EsplVar2.m` script. In this script, the comparison between these stresses and the admissible ones, obtained with `MaterialStrenght`, are used to assess the structural resistance of the blade.

A.2.6. StructuralAnalys

This function performs the structural analysis on the beam that connects two rotors. The beam has a symmetrical "H" section with parameters defined in input as in Figure 3.8. It allows to study beams of different materials, calculating the maximum stresses and comparing them with the admissible ones of the material. It also checks for compression instability. The inputs and outputs of this function are listed in Figure A.6. Among the required inputs there is the length of the beam expressed with `L` in this function. This variable is automatically calculated by the `EsplVar2.m` script starting from the radius of each rotor as already seen (`L`$= \ell = 2R + 1$). The section of the beam is defined with the parameters `b, b_a, h, h_a` as in Figure 3.8. Then it requires to define the position of the cable connections with respect to the parameters a and d (see section 3.1). To obtain similar structures, the `EsplVar2.m` script requires the variables `a_percent` and `gamma` from which, through the equations seen in section 3.1, it is possible to calculate the respective values of a and d. This is done in `EsplVar2.m` before calling the `StructuralAnalysis.m` function. This function also requires the `MaterialFile` string with the path to the file that

contains the properties of the material used for the beam. To carry out the structural analysis, the loads applied to the beam are also required, that are the thrust `T` and longitudinal force `H` but also the total weight of a rotor `W_rotor` (blades + generator) with also the applied electric torque `Q_e`. Finally, the `theta` vector is required. It is the vector produced in the `EsplVar.m` script, that contains all the θ angles at which the structure resistance and vertical equilibrium are assessed.

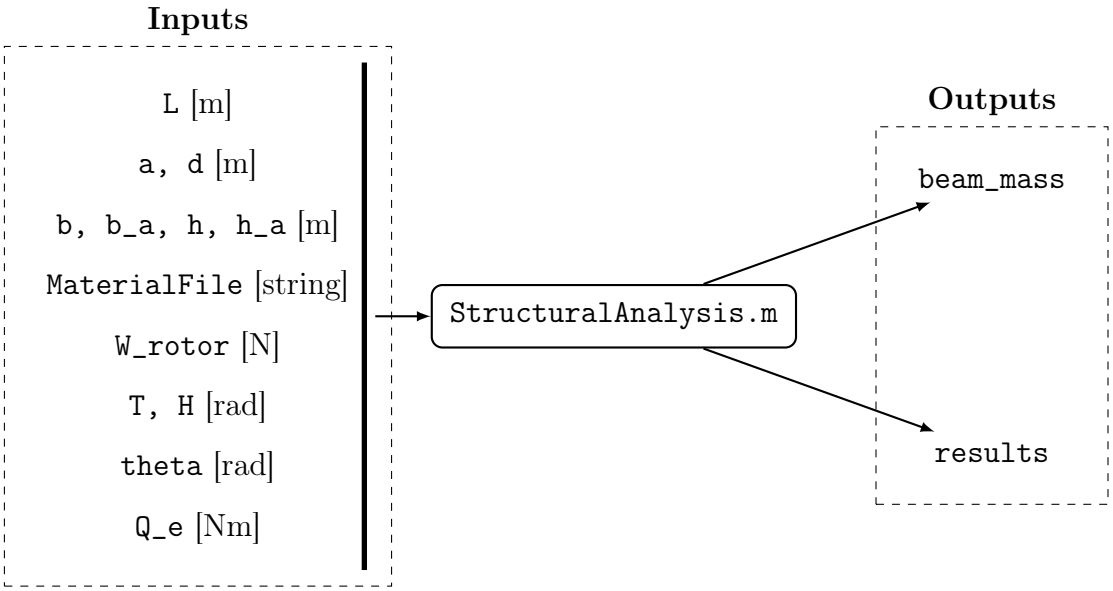

Figure A.6: Inputs and Outputs of `StructuralAnalysis.m`.

This function, produces two outputs that are the beam mass, used to assess the vertical equilibrium, and the results of the structural constraint over the beam. In particular, this last output is a vector that contains, for each θ angle of `theta` vector, the results of the structural constraint: positive if it has been passed or negative.

Finally, this function for structural analysis calls 2 functions for calculating the internal actions in the beam with respect to the ξ-z and η-z planes (see 3.2.2, 3.2.1) that are `InternalActionCsiZ.m` and `InternalActionEtaZ.m`. These two functions contain the structural model developed in chapter 3.

InternalActionEtaZ

The `InternalActionEtaZ.m` function is used to compute the internal action in the plane η-z. This function requires as input the variable `L` which represents the length of the beam with the parameters a and d which define the position of cable connections. It also requires all the loads applied to the structure which are the thrust of a rotor `FT` (so called

to distinguish it from the shear force T) and the longitudinal force `FH`. Also added are the `Q_e` electric torque and the weight of a rotor (`W_rotor`) and the weight of the structure `Ws`. Finally, the `theta` vector is also required. The outputs of this function are three. The `Zvect` that is a vector that contains the discretization of the blade span as required for RotorCS. Than the `Nvect` contains the axial force in each z position defined in `Zvect` while `Mvect` contains the flapping moment in each z position.

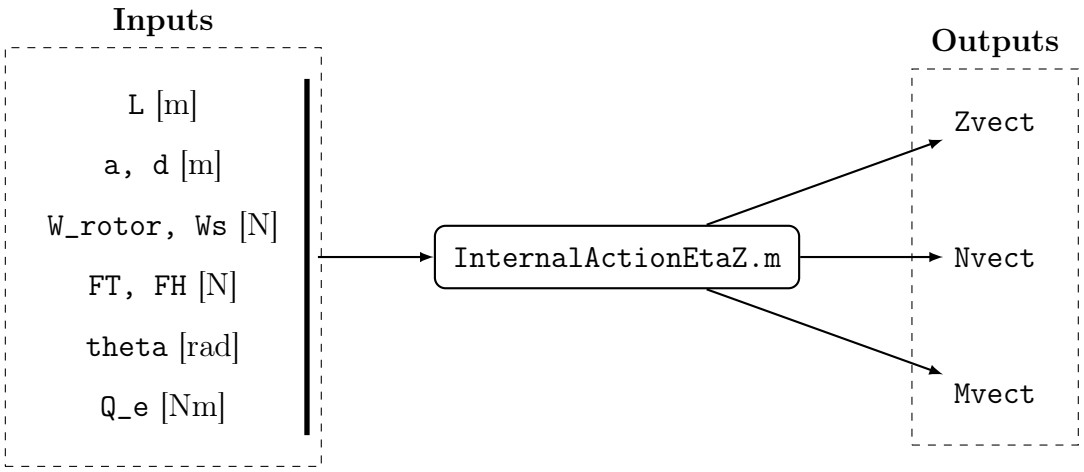

Figure A.7: Inputs and Outputs of `InternalActionEtaZ.m`.

InternalActionCsiZ

This function is similar to `InternalActionEtaZ.m` but it considers a different plane: the ξ-z. This function has the same input of the previous one but only one output. In fact, the vectors `Zvect` and `Nvect` are the same in both planes. The inputs and output of this last function are listed in Figure.

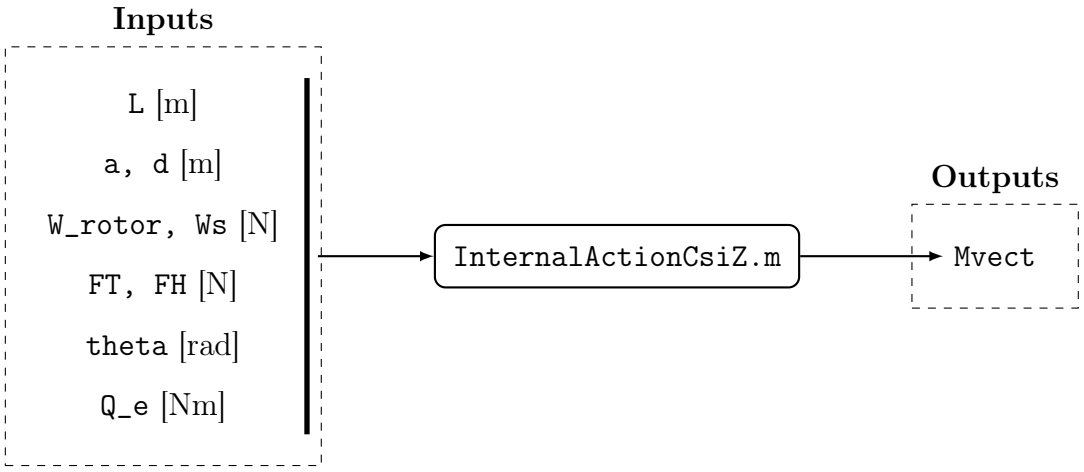

Figure A.8: Inputs and Outputs of `InternalActionCsiZ.m`.

List of Figures

List of Tables

List of Symbols

Variable	Description	SI unit
a	cable attachment distance from beam tip	m
A	beam section	m^2
b	width of beam section	m
b_a	width of beam web	m
B	number of rotor blades	-
c	airfoil chord	m
C_D	airfoil drag coefficient	-
C_L	airfoil lift coefficient	-
$C_{L_{/\alpha}}$	airfoil lift curve slope	rad^{-1}
d	cable bifurcation distance from the beam	m
d_b	blade element distance from the line joining the beginning and end of the blade	m
D	airfoil drag force	N
E	Young's modulus	MPa
F_D	rotor drag force	N
$\mathrm{F_F}$	cable tension	N
$\mathrm{F_{FB}}$	support reaction in point B of the beam	N
$\mathrm{F_{B}}_z$	z component of $\mathrm{F_{FB}}$	N
$\mathrm{F_{B}}_\eta$	η component of $\mathrm{F_{FB}}$	N
$\mathrm{F_{B}}_\xi$	ξ component of $\mathrm{F_{FB}}$	N
$\mathrm{F_{FC}}$	support reaction in point C of the beam	N
$\mathrm{F_{C}}_z$	z component of $\mathrm{F_{FC}}$	N
$\mathrm{F_{C}}_\eta$	η component of $\mathrm{F_{FC}}$	N
$\mathrm{F_{C}}_\xi$	ξ component of $\mathrm{F_{FC}}$	N
$\mathrm{F_H}$	total longitudinal force (2 rotors)	N

Variable	Description	SI unit
F_L	rotor lift force	N
$\mathrm{F_T}$	total thrust force (2 rotors)	N
F_y	vertical force on each blade	N
F_η	total force along η axis in point A and D of the beam	N
F_ξ	total force along ξ axis in point A and D of the beam	N
h	height of beam section	m
h_a	height of beam web	m
H	rotor longitudinal force	N
H_c	longitudinal force coefficient	-
I	second moment of area	m^4
$I_{\eta\eta}$	beam section moment of inertia with respect η axis	m^4
$I_{\xi\xi}$	beam section moment of inertia with respect ξ axis	m^4
k_D	rotor drag coefficient	-
k_L	rotor lift coefficient	-
ℓ	beam length	m
ℓ_E	effective length	m
L	airfoil lift force	N
M	bending moment	Nm
N	axial force	N
P	electrical power produced	W
P_d	wind power density	$\mathrm{W/m}^2$
q	distributed load on the blade	N/m
Q	shaft torque	Nm
Q_c	torque coefficient	-
Q_e	electrical torque	Nm
r	blade radial position	m
R	rotor radius	m
T	rotor thrust	N
T	shear force	N
T_c	thrust coefficient	-
T_d	thrust design value	N
u	effective axial velocity	m/s

Variable	Description	SI unit
U	wind speed relative to the airfoil	m/s
U_P	perpendicular component of U with respect the rotor plane	m/s
U_R	radial component of U	m/s
U_T	tangential component of U with respect the rotor plane	m/s
v_i	average induced velocity	m/s
V	required wind speed for steady state operation of autogyro	m/s
V_c	climb velocity	m/s
V_w	wind speed	m/s
W_B	blade weight	N
W_m	motor/generator weight	N
W_R	rotor weight	N
W_s	weight of the beam	N
W_{tot}	total weight of autorotational AWE	N
W_η	distributed weight of the beam along η axis	N/m
W_ξ	distributed weight of the beam along ξ axis	N/m
Y	rotor lateral force	N

Variable	Description	SI unit
α	pitch angle of blade section	rad
α_r	angle of attack of blade element in radial position r	rad
α_s	airfoil stall angle	rad
β	coning angle	rad
β_0, β_1, β_2	Fourier series parameters of flapping motion	rad
γ	semi-angle between two ropes after the cable bifurcation	rad
δ	mean airfoil drag coefficient	-
ϵ	cable inclination	rad
η_1, η_2	blade curvature parameters	-
θ	rotor angle of attack	rad
λ	tip speed ratio	-
λ_E	beam slenderness	-
μ	axial flow ratio	-
μ_c	constraint parameter	-
ν	induced axial velocity	m/s
ξ_1	blade curvature parameter	-
ρ	air density	kg/m^3
ρ_I	radius of gyration	m
σ	rotor solidity	-
σ_{cr}	critical stress	MPa
σ_N	axial stress	MPa
σ_y	yeld stress of material	MPa
σ_{zz}	axial stress	MPa
ϕ_r	inflow angle	rad
χ	blade curvature parameter	rad
ψ	rotor azimuth angle	rad
ψ_1, ψ_2	Fourier series parameters of flapping motion	rad
Ω	rotor angular speed	rad/s

Ringraziamenti

Questo lavoro rappresenta la conclusione di un lungo percorso di studi, composto da molti successi e grandi soddisfazioni ma non privo di difficoltà. Per tale motivo, colgo questa occasione per fare un bilancio di questi ultimi anni e ringraziare tutte quelle persone che non ho ringraziato abbastanza per essermi state vicine ed avermi sostenuto in questi anni.

Parto con il ringraziare la mia famiglia ed in particolare i miei genitori, senza i quali tutto ciò non sarebbe stato possibile. Li ringrazio per avermi dato questa grande opportunità e per avermi sostenuto e spinto ad andare avanti anche quando tutto sembrava andar male. So che siete orgogliosi di questo mio risultato e ciò lo rende un momento di ancora maggior valore.

Ringrazio tutti i miei nonni che, malgrado l'età, hanno atteso questo momento con tanta voglia di festeggiare. In quanto a te, nonno Franco, non ho mai avuto modo di conoscerti ma so che anche tu ne saresti stato estremamente orgoglioso.

Voglio ringraziare Laura, la mia compagna di vita, che mi ha supportato e sopportato in questi anni. Vorrei ringraziarla per aver saputo attenuare i momenti difficili, fornendo punti di vista più positivi, e allo stesso tempo dando più colore nei momenti di gioia.

Ringrazio Luigi e Danilo, compagni di triennale prima che i diversi percorsi ci dividessero. Un grande grazie va a Matteo, Mattia, Ludovico, Daniele e Omar: ottimi compagni di gruppo, e di serate, che mi hanno fatto capire l'importanza e la potenza della cooperazione. Molti degli ottimi risultati ottenuti sono anche merito vostro.

Ringrazio tutti i miei amici con cui ho passato bellissimi momenti e che mi hanno ricordato che esiste altro oltre al solo lavoro e insegnato a prendere la vita più alla leggera. Mi sento in particolare di ringraziare Leonardo e Marco per il tempo passato insieme, soprattutto nell'ultimo periodo, e per la condivisione di riflessioni e passioni che hanno contribuito alla mia crescita.

Sembrerà strano, ma sento di dover ringraziare anche la mia università: il Politecnico di Milano. La ringrazio per tutte le nozioni che ho avuto modo di imparare, per lo sviluppo dell'abilità di ragionamento e per avermi aperto la mente. Ho avuto modo di compren-

dere la vastità del bacino di conoscenza e questo ha contribuito allo sviluppo di umiltà nei confronti del sapere. Ringrazio soprattutto per tutti gli isegnamenti indiretti e non didattici ricevuti: è stato, infatti, un percorso di crescita oltre che di puro apprendimento.

Infine ringrazio me stesso per non aver mai mollato ed essere sempre andato avanti con lo scopo di raggiungere i miei obbiettivi. Con questo percorso ho capito che con costanza ed impegno, ogni obbiettivo può essere raggiunto. Ringrazio di aver dato il massimo, per aver continuato a cresce e migliorare e per essere arrivato dove sono ora. Continua così!

Ecco, questa tesi, come coronazione di questo percorso, è dedicata a tutti voi.

Luca Cominoli